

Plasmoid growth in 2D Full-F Gyrofluid Magnetic Reconnection

F. F. Locker,¹ M. Rinner,¹ M. Held,^{1,2} and A. Kendl¹

¹Department for Ion Physics and Applied Physics, University of Innsbruck, A-6020 Innsbruck, Austria

²Department of Mathematics and Statistics, UiT The Arctic University of Norway, 9037 Tromsø, Norway

(Dated: 9 March 2026)

Plasmoid growth is considered to enhance the rate of magnetic reconnection and is frequently used to explain fast magnetic reconnection in highly conductive (collisionless) plasmas. In strongly magnetized plasmas, the long wavelength dimension parallel to the magnetic field can be separated from the small wavelength perpendicular plane, justifying an isolated 2D approach. While 2D systems have been simulated using δF gyrofluids, a novel Full- F gyrofluid model with arbitrary wavelength polarization is used to simulate 2D Harris-sheet magnetic reconnection with domain aspect ratios $L_{\hat{y}}/L_{\hat{x}} \leq 16$ and investigate the corresponding plasmoid growth and tearing instability growth rates. In addition to linear tearing analysis, a non-modal stability analysis of the linearised system is performed. The evolution operator is shown to be strongly non-normal, exhibiting large condition numbers and extended pseudospectra, which indicate the possibility of significant transient amplification even in marginally stable regimes. This non-normal behavior provides a mechanism for explosive reconnection and helps explain the transition from linear tearing growth to rapid nonlinear acceleration. We focus on low plasma beta magnetic reconnection on the scale of the hybrid drift scale and incorporate ion finite Larmor radius (FLR) effects, putting the simulations in the perspective of magnetically confined nuclear fusion devices such as tokamaks. After discussing requirements on numerical resolution and convergence we present a parameter scan, varying the electron skin depth and the ion-to-electron temperature ratio. Finally, we present a discussion on the influence of aspect ratio, different models and possible contributions due to FLR effects.

I. INTRODUCTION

In magnetized plasmas, magnetic reconnection (MR) is known to play a crucial role in non-ideal magnetohydrodynamics (MHD), as magnetic field energy is converted into kinetic energy through the violation of flux conservation¹. This process is fundamental to a wide range of systems, including stellar coronae, Earth's magnetotail, and magnetically confined fusion devices^{2,3}. Since the early studies by Sweet and Parker, and later by Petschek, research has been extended from the comparatively well understood resistive MR regime to its collisionless counterpart, with the non-resistive tearing instability being identified as a key moderator of the process⁴⁻⁷.

Early theoretical descriptions predicted a decline of the resistive tearing instability growth rate $\gamma_{\eta} \sim S^{-3/3}$ with increasing Lundquist number $S = Lv_A/\eta$, where L denotes the characteristic system size, v_A the Alfvén velocity, and $\eta = (\mu_0\sigma)^{-1}$ the magnetic diffusivity, thereby limiting applicability to collisionless reconnection in the $\eta \rightarrow 0$ regime. It was later shown by Loureiro et al.⁸ that Sweet–Parker current sheets become unstable to secondary tearing via the plasmoid instability at sufficiently large values of $S \sim 10^4$, leading to enhanced linear growth rates as well as nonlinear interactions, and rendering plasmoid-driven reconnection nearly independent of $S^{7,9-12}$. Furthermore, plasmoid formation in such current sheets has been found to be independent of $\beta = \mu_0 p/B^2$, the ratio of plasma pressure p to magnetic pressure B^2/μ_0 , in the high- S regime¹³.

Current sheets thinner than an aspect ratio scaling as $a/L \sim S^{-1/3}$ (with a, L denoting the sheet width and length) were proposed by Pucci et al. to be inherently unstable, resulting in an “ideal” tearing mode characterized by reconnection

rates independent of S and explosive reconnection occurring on Alfvénic timescales¹⁴. In low- $\beta \ll 1$, high- S plasmas with large aspect ratios $r_a = a/L$, island formation involving multiple X-points (or magnetic nulls in three dimensions) has been shown to increase reconnection rates between coalescing flux surfaces by enabling multiple simultaneous reconnection sites through the plasmoid instability¹². A general theory based on a principle of least time was subsequently developed by Comisso et al., governing both the onset and dominant mode of the instability in evolving current sheets^{12,15}. It was demonstrated that plasmoid formation is not strictly governed by power-law scalings, but depends on system noise, resistivity, and current-sheet thinning rates. While the theory was later extended to include viscosity effects¹⁶. More recently, it was highlighted by Morillo et al.¹⁷ that plasmoid formation may be suppressed in numerical simulations if insufficient resolution is employed, even at high Lundquist numbers, underscoring the necessity of systematic convergence testing.

In toroidal geometry, such as tokamaks, the plasma is generally of high S , and resonant flux surfaces are known to be unstable to the tearing instability and subsequent island formation¹⁸. This is generally associated with a degradation of plasma confinement, as radial density profiles may be flattened and particles trajectories are shortcut. The interaction with turbulence, however, has been shown to be more complex^{15,19-23}. Although finite Larmor radius (FLR) effects are often negligible for marginally stable current sheets, both electron inertia and FLR effects have been shown to enable fast (explosive) reconnection under certain conditions²⁴⁻²⁷. Gyrofluid models have been demonstrated to retain the same collisionless mechanisms responsible for fast magnetic reconnection as kinetic simulations²⁸. Correspondingly, fast reconnection rates E_{rec} of order $E_{\text{rec}}/(B_0 v_A) \sim 0.1$, (background magnetic field density := B_0 , Alfvén velocity := v_A)

have been consistently reported in gyrokinetic, Hall-MHD, and fully kinetic simulations^{29–33}, particularly for moderately low electron skin depth $d_e = \sqrt{m_e/(\mu_0 e^2 n_e)}$ to drift scale $\rho_s = \sqrt{T_e m_i}/(eB_0)$ ratios, $d_e/\rho_s \approx 1$.

In the present work, the recently published code GREENY (Gyrofluid Reconnection with Extended Electromagnetic Nonlinearity)³⁴ is employed. GREENY is a two-dimensional Full-F gyrofluid simulation framework designed for the investigation of collisionless magnetic reconnection in parameter regimes relevant to fusion plasmas. The model constitutes a local slab approximation applicable to tokamak plasmas, while toroidal curvature, trapped-particle effects, and global equilibrium gradients are not included. Here, the term ‘‘collisionless’’ refers to the neglect of parallel resistive (e.g. Spitzer) terms, such that $\eta_S \rightarrow 0$, and reconnection is instead mediated by non-ideal effects such as inertia and numerical or hyper-viscosity. Arbitrary wavelength polarization is supported, and total densities are evolved self-consistently in time.

| | |
|-------------------------------|--|
| species temperature | T_z |
| species mass | m_z |
| charge number | Z_z |
| perpendicular gradient length | L_\perp |
| charge | $q_z := eZ_z$ |
| drift scale | $\rho_s := \sqrt{T_e m_i}/(eB_0)$ |
| electron skin depth | $d_e := \sqrt{m_e}/(\mu_0 e^2 n_e)$ |
| temperature ratio | $\tau_z := \frac{T_z}{Z_z T_e}$ |
| mass ratio | $\mu_z := \frac{m_z}{Z_z m_i}$ |
| electron beta | $\beta = \mu_0 N_e T_e / B_0^2$ |
| sound speed | $c_s := \sqrt{T_e/m_i}$ |
| $E \times B$ velocity | $ U_E = 1/B_0 \nabla_\perp \psi_z $ |
| perpendicular Poisson bracket | $1/B_0 (\hat{\mathbf{b}} \times \nabla_\perp f) \cdot \nabla g = 1/B_0 [f, g]_\perp$ |

TABLE I: Physical quantities, system parameters, and identities.

This formulation defines a Full-F, non-Oberbeck–Boussinesq (NOB) model, governed by the system parameters tab. I, with a constant species gyro-radius $\rho_z = \sqrt{T_e m_z}/(eB) = \text{const.}$ and a locally constant magnetic guide field $B = B_0$ ³⁵. Consequently, the model is isothermal and while densities are evolved as total quantities, the magnetic field evolution is of perturbative nature³⁶. A reduced Oberbeck–Boussinesq (δF) limit is also available, in which densities N_z are decomposed into a constant background N_0 and perturbations δN_z , and an OB-approximated polarization equation is employed for arbitrary wavelengths. Perpendicular magnetic field fluctuations are computed self-consistently via Ampère’s law. The numerical implementation and associated modeling assumptions are described in detail in Ref.³⁴. Both Full-F and δF magnetic reconnection can therefore be simulated, including first-order FLR effects for non-zero ion-to-electron temperature ratios $\tau_i = T_i/T_e \neq 0$. While δF models originate from linearized gyrokinetic formulations, Full-F models are derived from moment equations of the Full-F gyrokinetic Vlasov equation^{37,38}. The primary difficulty lies in the treatment of quasi-neutrality and

Ampère’s law, which necessitates additional approximations to obtain a closed system of equations; these approximations are discussed in Ref.³⁴.

Within the scope of this work, collisionless magnetic reconnection is investigated in the described gyrofluid framework, with a focus on parameter regimes characteristic of tokamak plasmas (e.g. low- β , $L_\perp \sim \rho_s$), thereby emphasizing ion-FLR effects. Following the presentation of the model equations in Section II, a linear perturbation analysis is performed in Section III A to derive the linear growth rate γ_{lin} of the tearing instability. Subsequently, the conditionality of the system is examined by means of a non-modal analysis in Section III B, with the aim of estimating intermittent tearing behavior. In Section IV, Harris-sheet magnetic reconnection is simulated in a square domain under different polarization assumptions, and δF and Full-F results for linear growth rates are compared against analytical predictions. Aspect-ratio effects on magnetic reconnection and plasmoid formation are also analyzed in Section IV, along with the influence of the normalized electron skin depth $\hat{d}_e = d_e/\rho_s = \sqrt{\mu_e}/\sqrt{\beta}$ over the range 10^{-4} to 10^3 and potential FLR contributions. Finally, conclusions and a summary of the results are provided in Section V.

II. MODEL EQUATIONS

A. Full-F collisionless MR model

The collisionless magnetic reconnection model, introduced in Ref.³⁴, is derived from the Full-F gyrofluid formulation of Madsen³⁷ together with Held et al.³⁹. For the sake of completeness, the model and its limits are presented again. The low- β limit, $\beta \ll 1$, of the Full-F model is considered, all curvature effects are neglected, and a uniform guide magnetic field $\mathbf{B} = B_0 \hat{\mathbf{e}}_\parallel$ is assumed. The evolution equations for the density and canonical momentum are

$$\begin{aligned} \frac{\partial}{\partial t} N_z + \frac{1}{B} [\psi_z, N_z]_\perp - N_z \frac{1}{B} [\xi_{1,z}, U_z]_\perp - U \frac{1}{B} [\xi_{1,z}, N_z]_\perp &= \Lambda \\ \frac{m_z N_z}{q_z} \frac{\partial}{\partial t} U_z + N_z \frac{\partial}{\partial t} \xi_{1,z} &= \\ = -\frac{m_z N_z}{q_z B} [\psi_z, U_z]_\perp + N_z \frac{1}{B} [\xi_{1,z}, \psi_z]_\perp + \frac{m_z U_z N_z}{q_z B} [\xi_{1,z}, U_z]_\perp + \frac{T_z}{q_z B} [\xi_{1,z}, N_z]_\perp \end{aligned}$$

for each species, where $\psi_{1,z} := \Gamma_{1,z} \phi$ and $\xi_{1,z} := \Gamma_{1,z} A_\parallel$. These evolution equations are normalized (denoted by $\hat{\cdot}$) according to the Bohm normalization scheme shown in Table II.

The corresponding system constants and parameters are listed in Table I. We decompose the magnetic-field unit vector as $\hat{\mathbf{b}} = \hat{\mathbf{b}} + \tilde{\mathbf{b}}$, where the fluctuating component is given by $\tilde{\mathbf{b}} = \frac{1}{B_0} \nabla A_\parallel \times \hat{\mathbf{b}}$. The normalized parallel gradient of a field \hat{f} becomes

$$\hat{\nabla}_\parallel \hat{f} := \hat{\nabla}_\parallel \hat{f} + \tilde{\mathbf{b}} \cdot \hat{\nabla} \hat{f} = \hat{\nabla}_\parallel \hat{f} - \frac{\beta}{\hat{B} \hat{\delta}} [\hat{A}_\parallel, \hat{f}]_\perp \quad (1)$$

| | |
|---------------------------------|--|
| time | $t := \frac{L_\perp}{c_s} \hat{t}$ |
| gyrocenter number density | $N_z := N_0 \hat{N}_z$ |
| Poisson bracket | $\{\cdot, \cdot\}_\perp := \rho_s^{-2} [\cdot, \cdot]_\perp$ |
| magnetic-field magnitude | $B := B_0 \hat{B}$ |
| generalized electric potential | $\psi_z := \frac{L_e}{e} \hat{\psi}$ |
| parallel velocity | $U_z := c_s \hat{U}_z$ |
| parallel vector potential | $A_\parallel := (B_0 \rho_s) \hat{A}_\parallel$ |
| perpendicular gradient operator | $\nabla_\perp := \rho_s^{-1} \hat{\nabla}_\perp$ |

TABLE II: Bohm normalization scheme of the dependent fields.

where the second term is magnetic flutter. In this normalization, the parameter $\delta = \rho_s/L_\perp$ scales the Poisson brackets and hence the system dynamics. Since the characteristic gradient length is of order ρ_s , the dimensionless scaling parameter is set to $\delta = 1$. The gyrocenter $E \times B$ drift is determined by the gyroaveraged and polarization components of the gyrofluid potential $\hat{\psi}_z = \hat{\psi}_{1,z} + \hat{\psi}_{2,z}$ ⁴⁰,

$$\hat{\psi}_{1,z} := \hat{\Gamma}_{1,z} \hat{\phi}, \quad (2)$$

$$\hat{\psi}_{2,z} := -\frac{\mu_z}{2} \left| \hat{\nabla}_\perp \sqrt{\hat{\Gamma}_{0,z}} \hat{\phi} \right|^2. \quad (3)$$

The exact form of the operators depends on the model assumptions summarized in Table III. For the remainder of this work, β is absorbed into $\hat{A}_\parallel = \beta \hat{A}_\parallel$. The Padé-approximated gyroaverage and screening operators are³⁹

$$\hat{\Gamma}_{0,i} := \frac{1}{1 - \tau_i \mu_i \hat{\Delta}_\perp}, \quad \hat{\Gamma}_{1,i} := \frac{1}{1 - \frac{\tau_i}{2} \mu_i \hat{\Delta}_\perp}. \quad (4)$$

Since $|\mu_e| \ll 1$ for proton–electron plasmas, electron FLR effects may be neglected, which implies $\hat{\psi}_e = \hat{\phi}$, $\hat{\Gamma}_{0,e} = \hat{\Gamma}_{1,e} = 1$, $\hat{N}_e = \hat{n}_e$ and $\hat{U}_e = \hat{u}_e$. The normalized and implemented Full-F equations are

$$\frac{\partial}{\partial \hat{t}} \hat{n}_e = - [\hat{\phi}, \hat{n}_e]_\perp + [\hat{A}_\parallel, \hat{n}_e \hat{u}_e]_\perp, \quad (5)$$

$$\frac{\partial}{\partial \hat{t}} \hat{N}_i = - [\hat{\psi}_i, \hat{N}_i]_\perp + [\hat{\Gamma}_1 \hat{A}_\parallel, \hat{N}_i \hat{U}_i]_\perp, \quad (6)$$

$$\begin{aligned} \frac{\partial}{\partial \hat{t}} \left(\hat{u}_e + \frac{1}{\mu_e} \hat{A}_\parallel \right) = & - \left[\hat{\phi}, \hat{u}_e + \frac{1}{\mu_e} \hat{A}_\parallel \right]_\perp + \\ & + \left[\hat{A}_\parallel, \frac{1}{2} \hat{u}_e^2 \right]_\perp - \frac{1}{\mu_e} \left[\hat{A}_\parallel, \ln(\hat{n}_e) \right]_\perp, \end{aligned} \quad (7)$$

$$\begin{aligned} \frac{\partial}{\partial \hat{t}} \left(\hat{U}_i + \hat{\Gamma}_1 \hat{A}_\parallel \right) = & - \left[\hat{\psi}_i, \hat{U}_i + \hat{\Gamma}_1 \hat{A}_\parallel \right]_\perp + \\ & + \left[\hat{\Gamma}_1 \hat{A}_\parallel, \frac{1}{2} \hat{U}_i^2 \right]_\perp + \tau_i \left[\hat{\Gamma}_1 \hat{A}_\parallel, \ln(\hat{N}_i) \right]_\perp. \end{aligned} \quad (8)$$

With the $\mathbf{E} \times \mathbf{B}$ drift and the perpendicular magnetic flutter 1, the species advection velocities are

$$\mathbf{V}_e := \mathbf{u}_E + u_e \tilde{\mathbf{b}}, \quad (9)$$

$$\mathbf{V}_i := \mathbf{u}_E + U_i \tilde{\mathbf{b}}. \quad (10)$$

where $\nabla \cdot \mathbf{V}_z = 0$. Hence, the equations in advective form are

$$\frac{\partial}{\partial \hat{t}} n_e = -\mathbf{V}_e \cdot \nabla n_e - n_e \tilde{\mathbf{b}} \cdot \nabla u_e, \quad (11)$$

$$\frac{\partial}{\partial \hat{t}} N_i = -\mathbf{V}_i \cdot \nabla N_i - N_i \tilde{\mathbf{b}} \cdot \nabla U_i \quad (12)$$

$$\frac{\partial}{\partial \hat{t}} \left(\hat{u}_e + \frac{1}{\mu_e} \hat{A}_\parallel \right) = -\mathbf{V}_e \cdot \nabla u_e + \frac{1}{\mu_e} \tilde{\mathbf{b}} \cdot \nabla (\ln n_e - \phi), \quad (13)$$

$$\frac{\partial}{\partial \hat{t}} \left(\hat{U}_i + \hat{\Gamma}_1 \hat{A}_\parallel \right) = -\mathbf{V}_i \cdot \nabla U_i - \tau_i \tilde{\mathbf{b}} \cdot \nabla \ln N_i - \tilde{\mathbf{b}} \cdot \nabla \psi. \quad (14)$$

Here we used $\hat{N}_e \approx \hat{n}_e$ and $\hat{U}_e \approx \hat{u}_e$, valid for electron mass ratios $|\mu_e| \ll 1$ at ρ_s scales and small β . This regime is characteristic of fusion plasma simulations dominated by drift-wave dynamics interacting with reconnecting magnetic field structures. While in a turbulent setting, the implementation of equations 5 requires a subgrid dissipation^{41–43} one generally also needs regularization for centered differencing. This is done by transforming

$$\frac{\partial}{\partial \hat{t}} \rightarrow \frac{\partial}{\partial \hat{t}} + \nu \hat{\nabla}_\perp^4. \quad (15)$$

For the problem of magnetic reconnection one can either take the numerical diffusion into account²⁷ or choose the scalar parameter ν small enough to prevent a strong influence on the reconnecting current sheet³⁴. In the presented setting, a small hyperviscosity parameter of $\nu \propto 10^{-6}, 10^{-7}$ is used, further discussed in III C.

The system is closed by Ampère's law,

$$-\frac{1}{\beta} \hat{\Delta}_\perp \hat{A}_\parallel = -\hat{n}_e \hat{u}_e + \hat{\Gamma}_1 (\hat{N}_i \hat{U}_i), \quad (16)$$

and the arbitrary-wavelength, non-Oberbeck–Boussinesq (NOB) polarization equation,

$$\hat{\nabla} \cdot \left[\sqrt{\hat{\Gamma}_0} \frac{\hat{N}_i}{\hat{\beta}^2} \sqrt{\hat{\Gamma}_0} \hat{\nabla}_\perp \hat{\phi} \right] = -\sum_z Z_z \hat{\Gamma}_{1,z} \hat{N}_z. \quad (17)$$

The polarization equation may be written as

$$\sum_z Z_z \hat{N}_z - \hat{\nabla} \cdot \hat{\mathbf{P}} = 0, \quad (18)$$

where $\hat{\mathbf{P}} = \hat{\mathbf{P}}_1 + \hat{\mathbf{P}}_2$ ^{35,40} and

$$\hat{\mathbf{P}}_1 := -\sum_z Z_z \hat{\nabla}_\perp \hat{\Gamma}_{1,z} (\mu_z \tau_z \hat{N}_z / 2), \quad (19)$$

$$\hat{\mathbf{P}}_2 := -\sum_z \left(\sqrt{\hat{\Gamma}_{0,z}} Z_z \mu_z \frac{\hat{N}_z}{\hat{\beta}^2} \sqrt{\hat{\Gamma}_{0,z}} \hat{\nabla}_\perp \hat{\phi} \right). \quad (20)$$

Here the second-order Padé approximation $\hat{\Gamma}_1 \approx \sqrt{\hat{\Gamma}_0}$ is used³⁹, together with

$$-\hat{\nabla} \cdot \hat{\mathbf{P}}_1 = \sum_z Z_z (\hat{\Gamma}_1 - 1) \hat{N}_z. \quad (21)$$

The respective OB and LWL approximation of the polarization equation are summed up in table III. The normalized total energy is

$$\hat{E}_{\text{tot}} = \sum_z \int_V dV \left(Z_z \tau_z \hat{N}_z \ln(\hat{N}_z) - Z_z \hat{N}_z \hat{\psi}_{2,z} + Z_z \mu_z \frac{1}{2} \hat{N}_z \hat{U}_z^2 + \frac{|\hat{V}_\perp \hat{A}_\parallel|^2}{2\beta} \right) \quad (22)$$

which consists of the Helmholtz free energy \hat{E}_n , the $E \times B$ energy $\hat{E}_{E \times B}$, the parallel energy \hat{E}_\parallel , and the perturbed magnetic energy \hat{E}_m . The chosen normalization targets turbulence at the scale of ρ_s , thereby defining the resolvable range of fluctuations and implying that only ion FLR effects are retained. These effects become significant mainly in large-aspect ratio systems and in turbulent magnetic-reconnection scenarios²⁷.

B. Oberbeck-Boussinesq approximated equations

One can recover the OB (δF) limit, assuming a constant background density N_0 and small perturbations \hat{N}_z , substituting $\hat{N}_z = 1 + \hat{N}_z$ in the Full-F equations³⁸. Further simplification is obtained by assuming $\hat{n}_z \ll \hat{N}_0$ (or, in normalized form, $\hat{n}_z \ll 1$), neglecting triple non-linearities and employing the δF polarization equation.

$$\frac{\partial}{\partial t} \hat{n}_e = - [\hat{\phi}, \hat{n}_e]_\perp + [\hat{A}_\parallel, \hat{u}_e]_\perp, \quad (23)$$

$$\frac{\partial}{\partial t} \hat{N}_i = - [\hat{\psi}, \delta \hat{N}_i]_\perp + [\hat{\Gamma}_1 \hat{A}_\parallel, \hat{U}_i]_\perp, \quad (24)$$

$$\frac{\partial}{\partial t} \left(\hat{u}_e + \frac{1}{\mu_e} \hat{A}_\parallel \right) = - \left[\hat{\phi}, \hat{u}_e + \frac{1}{\mu_e} \hat{A}_\parallel \right]_\perp - \quad (25)$$

$$- \frac{1}{\mu_e} [\hat{A}_\parallel, \hat{n}_e]_\perp, \quad (26)$$

$$\frac{\partial}{\partial t} \left(\hat{U}_i + \hat{\Gamma}_1 \hat{A}_\parallel \right) = - [\hat{\psi}, \hat{U}_i + \hat{\Gamma}_1 \hat{A}_\parallel]_\perp + \quad (27)$$

$$+ \tau_i [\hat{\Gamma}_1 \hat{A}_\parallel, \hat{N}_i]_\perp, \quad (28)$$

$$- \frac{1}{\beta} \hat{\Delta}_\perp \hat{A}_\parallel = - \hat{u}_e + \hat{\Gamma}_1 (\hat{U}_i), \quad (29)$$

$$\frac{1}{\tau_i} (\hat{\Gamma}_0 - 1) \hat{\phi} = \hat{n}_e - \hat{\Gamma}_1 \hat{N}_i \quad (30)$$

Note, that the Full-F and Full-F + OB polarization equations coincide only in their respective long-wavelength limit (LWL) (Table III). These equations match the model derived by Scott³⁸. A key difference between the Full-F and Full-F + OB systems is the presence of cubic nonlinearities in all evolution equations.

| GF model | $\hat{\mathbf{P}}_2$ | $\hat{\psi}_2$ |
|-------------------|--|---|
| Full-F | $-\sum_z \sqrt{\hat{\Gamma}_0} \mu_z Z_z \frac{\hat{N}_z}{\hat{B}_0^2} \sqrt{\hat{\Gamma}_0} \hat{V}_\perp \hat{\phi}$ | $-\mu_z \hat{V}_\perp \sqrt{\hat{\Gamma}_0} \hat{\phi} ^2$ |
| Full-F + OB | $-\sum_z \mu_z Z_z \frac{\hat{N}_z}{\hat{B}_0^2} \hat{\Gamma}_0 \hat{V}_\perp \hat{\phi}$ | 0 |
| Full-F + LWL | $-\sum_z \mu_z Z_z \frac{\hat{N}_z}{\hat{B}_0^2} \hat{V}_\perp \hat{\phi}$ | $-\mu_z \hat{V}_\perp \hat{\phi} ^2$ |
| Full-F + OB + LWL | $-\sum_z \mu_z Z_z \frac{\hat{N}_z}{\hat{B}_0^2} \hat{V}_\perp \hat{\phi}$ | 0 |

TABLE III: Long wavelength (LWL) and Oberbeck-Boussinesq (OB) approximation of the polarization density $\hat{\mathbf{P}}_2$ and polarization part of the gyrofluid potential $\hat{\psi}_2$ for different models.

III. STABILITY ANALYSIS

A. Linearized System of Equations

To obtain an analytical estimate $\hat{\gamma}_{\text{in}}$ for the tearing instability growth rate $\hat{\gamma}$, the approach of Tassi et al.⁴⁴ is followed. The Full-F equations are linearized in the cold-ion limit $\tau_i = T_i/T_e \approx 0$, whereby the gyroaveraging operators $\hat{\Gamma}_1$ and $\hat{\Gamma}_0$ are eliminated (yielding, for example, $\hat{\psi} = \hat{\phi}$). A harmonic ansatz of the form

$$F(x, y, t) = F_{\text{eq}}(x) + \tilde{F}(x) \exp(i(ky - \omega t)),$$

with $\omega = i\gamma$ and F representing one of the six fields, is employed. The analysis is restricted to the small-growth-rate regime $\gamma \ll 1$, using the following equilibrium functions, which are characteristic of a Harris-sheet initial condition.

$$\hat{n}_{e,\text{eq}}(x) = N_0 = \text{const.}, \quad (31)$$

$$\hat{N}_{i,\text{eq}}(x) = N_0, \quad (32)$$

$$\hat{U}_{e,\text{eq}}(x) = \frac{1}{\beta N_0} \nabla_\perp^2 A_{\parallel,\text{eq}}(x), \quad (33)$$

$$\hat{U}_{i,\text{eq}}(x) = 0, \quad (34)$$

$$\hat{\phi}_{\text{eq}}(x) = 0, \quad (35)$$

$$\hat{A}_{\parallel,\text{eq}}(x) = \beta A_0 a_{\parallel,\text{eq}}(x) = -\beta A_0 \ln(\cosh(x)), \quad (36)$$

Analogous to^{44,45} an analytical estimate for the tearing stability parameter Δ' , in the marginally stable limit $\Delta' \ll 1$, is obtained (Appendix V A), by matching the inner and outer solution

$$\begin{aligned} \Delta'_{\text{outer}} &= 2 \left(\frac{1}{\hat{k}_y} - \hat{k}_y \right) = \Delta'_{\text{inner}} = \\ &= \beta N_0 \sqrt{\left(\frac{\hat{\gamma}_{\text{in}}}{A_0 \hat{k}_y} \right) \left[\frac{2.12}{\sqrt{\beta}} + \pi \left(\frac{1/\phi + \mu_e N_0^2}{-\mu_e N_0^2} \right) \left(\frac{\hat{\gamma}_{\text{in}} - \mu_e N_0^2}{\lambda} \frac{1}{A_0 \hat{k}_y} \right)^{1/2} \right]} \end{aligned} \quad (37)$$

where, $\lambda = \beta^2 (A_0^2 \mu_e + N_0^2)$ and, in the presented orientation, \hat{k}_y is the normalized wave number in \hat{y} direction. This expression can be inverted point-wise for values of \hat{k}_y and β to obtain

$\hat{\gamma}_{\text{lin}}$. For small $\beta < 10^{-2}$ the growth rate grows with β , which is in disagreement with three-dimensional simulations from Biancalani et al.²⁷ but, as a general trend, agrees with Tassi et al.⁴⁴ Further, the behavior for large β (figure 1) agrees somewhat with pressure-dominated scenarios described in^{46,47}. We point out that the derivation of the presented models imposes a low- β approximation, hence deviations at $\beta \sim 1$ are expected.

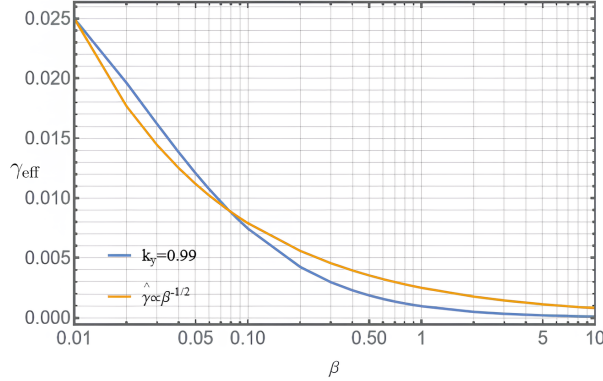


FIG. 1: The linear growth rate $\hat{\gamma}_{\text{lin}}$ at marginal stability as a function of β . The growth rate declines approximately as $\beta^{-1/2}$, predicted for large pressure dominated regimes.

One has to note that this solution for the growth rate is very much dependent on the equilibrium function \tilde{A}_{\parallel} , and a deviation has to be expected when e.g.

$$a_{\parallel,eq}(x) = \frac{1}{\cosh^2(x)} \quad (38)$$

is used. Such initial conditions are very suitable for implementation due to their boundary behavior, and we expect them to behave as analytically predicted in the linear regime due to the similarity in Δ' .

To translate the analytical result to the simulations we introduce the box-stability parameter Δ'_{box}

$$\Delta'_{\text{box}} = \lim_{x \rightarrow 0^+} \frac{\tilde{A}'_{\parallel, \text{out}}}{\tilde{A}_{\parallel, \text{out}}} - \lim_{x \rightarrow 0^-} \frac{\tilde{A}'_{\parallel, \text{out}}}{\tilde{A}_{\parallel, \text{out}}} = 2 \left(\frac{1}{\hat{k}} - \hat{k} \right) \quad (39)$$

where the Box size enters via $\hat{k}_{\hat{y}} = \pi m / L_{\hat{y}}$. To get e.g. $\hat{k}_{\hat{y}} = 1$ with $L_{\hat{y}} = 10\pi$ one needs $m = 10$, which results in a stability parameter of $\Delta'_{\text{box}} = 14.3108$. To obey the limits of the linear stability analysis the system is perturbed with a suitable mode number, close to marginal stability. Note that the aspect ratio $L_{\hat{y}} / L_{\hat{x}}$ does not explicitly show up in the dispersion relation, but as $L_{\hat{y}}$ enters via $\hat{k}_{\hat{y}}$ a change in the aspect ratio results in a different stability parameter. As a result of the small x approximation, rooted in the shrinking automatism of the current sheet, the initial k_x should not influence the general stability of the current sheet, while the aspect ratio of the sheet (note: not the box) still changes. This, and the general stability behavior

will be investigated in the following sections with the goal of code verification. A wide scan of aspect-ratio effects is left for later work.

B. Non-modal Analysis

If a system's evolution matrix \mathcal{A} is non-normal, the non-orthogonality of its eigenvectors makes typical spectral analysis less useful^{48,49}. While the evolution function $\|e^{t\mathcal{A}}\|$, with time t , decays monotonously for \mathcal{A} , the same only holds true for \mathcal{B} in the limit $t \rightarrow \infty$. In the early phase of the evolution, \mathcal{B} will undergo a transient phase, where the evolution function will develop a local maximum before decaying eventually. As a simple quantification of such a behavior, one can analyze the condition number

$$\kappa(V) = \|V\| \|V^{-1}\|$$

with V being a matrix of eigenvectors of the evolution matrix \mathcal{A} , to a solution of a differential equation

$$\frac{\partial u(x,t)}{\partial t} = \mathcal{A}u(x,t) \quad \rightarrow \quad u(x,t) = u(x,0)e^{t\mathcal{A}}.$$

While for a normal matrix \mathcal{A} , the norm of the system evolution³⁶

$$\frac{\|v(t)\|}{\|v(0)\|} \leq \|e^{\mathcal{A}t}\| \quad (40)$$

is bounded by the spectral abscissa $\beta(\mathcal{A}) = \max_k \{\text{Re}(\Lambda(\mathcal{A}))\}$, $\Lambda(\mathcal{A})$ denoting the spectrum and $\omega(\mathcal{A})$ the eigenvalues of \mathcal{A} , a non-normal matrix behaves like

$$\|e^{\mathcal{A}t}\| = \kappa(V)e^{\beta(\mathcal{A})t} \quad (41)$$

which only behaves normally for large t . As κ is a very conservative (large) upper bound for the system evolution, connected estimates are not really useful. While an estimate for the upper bound for the behavior at $t = 0$ can be calculated via the numerical abscissa⁵⁰

$$\eta(\mathcal{A}) := \max_k \{\omega[\mathcal{A}^\dagger + \mathcal{A}]/2\}, \quad (42)$$

another estimate for the transient behavior can be found via the ε -pseudospectral abscissa

$$\alpha_\varepsilon(\mathcal{A}) = \sup_{z \in \Lambda_\varepsilon(\mathcal{A})} \text{Re}(z), \quad (43)$$

which is defined via III.1 (see further below). To find the evolution matrix of the linearized system II the equations are rewritten in terms of the canonical momentum $A^* = \frac{1}{\mu_e} A_{\parallel} + u_e$. When \mathcal{A} is normal, the conditioning number κ is 1, while $\kappa = \infty$ in the case of a non diagonalizable matrix. Any quantitative analysis of the matrix \mathcal{A} , based on eigenvalues is then only valid up to a factor of κ . Such an analysis is often called "non-modal" and has been carried out in similar context (e.g. Hasegawa-Wakatani model) in various publications^{36,51-53}.

The transient non-modal growth of the tearing instability has been studied, and transient phases with faster magnetic reconnection have been repeatedly found for corresponding initial conditions^{24,27,54,55}. A modal analysis of the linearized Full-F model⁵⁶ is performed to study any transient behavior. Algebraic manipulations are carried out using Wolfram Mathematica (v. 12.3)⁵⁷. First, a simplified case with an initial condition $\hat{A}_{\parallel,eq} = a_0 x$ and constant gradient a_0 is considered, for which u_e and its derivatives vanish. The resulting evolution matrix reads

$$\mathcal{A}_{const.} = \begin{pmatrix} a_0 \kappa & 0 & a_0 \kappa \hat{k}_y - \frac{a_0 \kappa}{\alpha} & \frac{a_0 \kappa}{\alpha} \\ 0 & \frac{a_0 \kappa}{\alpha} & \frac{a_0 \kappa \mu_e}{\alpha} - \frac{a_0 \kappa \hat{k}_y \mu_e}{\alpha} & \frac{a_0 \kappa}{\alpha} \\ -\frac{a_0 \kappa}{\alpha} - \frac{ia_0 \hat{k}_y}{k_x^2 + \hat{k}_y^2} & \frac{ia_0 \hat{k}_y}{k_x^2 + \hat{k}_y^2} & 0 & 0 \\ -\frac{ia_0 \hat{k}_y}{\mu_e (k_x^2 + \hat{k}_y^2)} & \frac{ia_0 \hat{k}_y}{\mu_e (k_x^2 + \hat{k}_y^2)} & 0 & 0 \end{pmatrix}$$

If the initial A_{\parallel} (and obviously u_e etc.) has a spectrum on its own, one has to carry out the cyclic convolution for the product terms e.g.

$$\mathcal{F}(\hat{A}_{\parallel,0} \cdot \frac{\partial}{\partial y} n_e) = (2\pi)^{-\frac{n}{2}} \mathcal{F}(\hat{A}_{\parallel,0}) * \mathcal{F}(\frac{\partial}{\partial y} n_e).$$

Again, the solution depends on the initial vector potential $\hat{A}_{\parallel,0}$ (determining all the dependent quantities) and one option is to make use of the Fourier-sum representation, singling out one mode number so

$$\mathcal{F}(\hat{A}_{\parallel,0}) = \mathcal{F}(a_0 \cos(mx)) = a_0 \sqrt{\frac{\pi}{2}} (\delta(k-m) + \delta(m+k)).$$

One can finally use the sifting property of the convolution

$$\int_{-\infty}^{\infty} f(x) \delta(x-m) = f(m)$$

to obtain an evolution matrix for each mode number m .

The resulting eigensystem 2 can then be analyzed for different initialisations with mode number m , varying β and $k_{x,y}$. At this point it makes sense to single out a low \hat{k}_y and compare a few different values to investigate how the condition number scales with the system parameters. For $\hat{k}_y = 0$ the conditioning number is constantly $\kappa = 10^6$ for all parameters, and generally large for $\hat{k}_y \neq 0$ with a local minimum around marginal stability, yielding a possible explanation for transient behavior.

To analyze the spectrum of the evolution operator \mathcal{A} , making use of the resolvent of $\mathcal{A} \in \mathbb{C}^{n \times n}$

$$\mathcal{R}(\mathcal{A}) = (z\mathbb{I}_n - \mathcal{A})^{-1} \quad (44)$$

which is obviously singular when z is an eigenvalue $\lambda_{\mathcal{A}}$ of the operator. In the same way, we can define the spectrum of the operator $\Lambda(\mathcal{A})$ as the set of all values for which the resolvent becomes singular. Analogously one can define the ε pseudospectrum $\Lambda_{\varepsilon}(\mathcal{A})$ as the set of complex numbers that satisfy definition III.1⁴⁸.

Definition III.1 (ε -pseudospectrum).

The set of complex numbers z , that satisfy

- (i) $\|(z\mathbb{I}_n - \mathcal{A})^{-1}\| \geq \varepsilon^{-1}$,
- (ii) $\sigma_{min}(z\mathbb{I}_n - \mathcal{A}) \leq \varepsilon$, where σ_{min} denotes the smallest singular value,
- (iii) $\|\mathcal{A}u - zu\| \leq \varepsilon$ for some vector u with $\|u\| = 1$,
- (iv) z is an eigenvalue of $\mathcal{A} + E$, where E is a perturbation to \mathcal{A} with $\|E\| \leq \varepsilon$.

are called, the epsilon-pseudospectrum of Operator A .

In a practical sense, one can now plot ε -contour lines of $(z\mathbb{I}_n - \mathcal{A})$, which, in terms of the spectrum, means, that we can look at the subsets of "almost" singular values, and this ε -pseudospectrum can be viewed as the spectrum of some perturbed matrix. Nevertheless, the pseudospectrum does not only contain information about a change in the spectrum under a perturbation of the operator but also gives information about the operator itself⁵⁸. The pseudospectrum can be used to gain insight on transient effects on instabilities, and further, one can try to find parameters for the operator to prevent such transient behavior. In figure 3, the ε -spectrum of \mathcal{A} , together with the numerical abscissa (blue dotted line) is shown for an initial condition with $m = 1$ and one can see that the eigenvalues obey the upper bound at $t = 0$. For $\hat{k}_y \geq 1$ the complex eigenvalues vanish, and they increasingly shift to the positive real axis, including the 0-eigenvalue, and hence the stable case. The ε -pseudospectra extend deep into the unstable half-plane despite stable eigenvalues, indicating strong non-normality and the presence of transient growth. The numerical abscissa is positive for all \hat{k}_y considered, implying the existence of initial conditions with short-time exponential amplification. From the extent of the ε -pseudospectra, transient growth factors of order $1/\varepsilon$ are expected. This provides a natural explanation for the observed intermittent and explosive reconnection dynamics.

One may estimate transient growth by sampling perturbation matrices E with $\|E\| = \varepsilon \rightarrow 0$ and evaluating the corresponding spectral abscissa⁴⁸,

$$\gamma(A) = \lim_{\varepsilon \rightarrow 0} \alpha_{\varepsilon}(A). \quad (45)$$

Equivalently, one may infer bounds on transient growth directly from the ε -pseudospectrum by considering the rightmost extent of $\Lambda_{\varepsilon}(A)$ in the complex plane. For $\hat{k}_y \leq 1$, the largest observed values of $\alpha_{\varepsilon}(A)$ are approximately 0.2, which provides a more realistic upper bound on the transient growth rate than that suggested by the condition number alone.

In the present analytical estimate, a very simple class of initial conditions has been employed. In practice, however, the dynamics may involve more complex perturbations, and it is therefore not surprising if estimates based on a restricted set of modes (e.g. a fixed mode number) do not quantitatively match numerical simulations.

$$\mathcal{A}_m = \begin{pmatrix} \frac{\beta m \hat{k}_y (\mu_e (2k_x^2 + 2\hat{k}_y^2 - \sqrt{2\pi} m^4 - 2) + \sqrt{2\pi} m^2 + 2)}{4\mu_e (k_x^2 + \hat{k}_y^2 - 1) + 4} & 0 & \frac{\beta m \mu_e \hat{k}_y (k_x^2 + \hat{k}_y^2 + m^2 - 1)}{2\mu_e (k_x^2 + \hat{k}_y^2 - 1) + 2} & \frac{\beta m \hat{k}_y (1 - m^2 \mu_e)}{2\mu_e (k_x^2 + \hat{k}_y^2 - 1) + 2} \\ \frac{\sqrt{\frac{\pi}{2}} \beta m^3 \mu_e \hat{k}_y}{2\mu_e (k_x^2 + \hat{k}_y^2 - 1) + 2} & \frac{1}{2} \beta m \hat{k}_y & -\frac{\beta m \mu_e \hat{k}_y}{2\mu_e (k_x^2 + \hat{k}_y^2 - 1) + 2} & \frac{1}{2} \beta m \hat{k}_y \left(\frac{\mu_e}{\mu_e (k_x^2 + \hat{k}_y^2 - 1) + 1} + 1 \right) \\ \frac{1}{4} \left((2\pi\beta - i)\mu_e + \beta \left(\frac{4\pi}{\mu_e + 1} - 4\pi + 2 \right) + i \right) & \frac{1}{4} i (\mu_e - 1) & -\frac{\sqrt{\frac{\pi}{2}} \beta \mu_e}{\mu_e + 1} & \frac{\sqrt{\frac{\pi}{2}} \beta (\mu_e - 1) \mu_e}{2(\mu_e + 1)} \\ -\frac{i \hat{k}_y}{2(k_x^2 + \hat{k}_y^2)} & -\frac{i \hat{k}_y}{2(k_x^2 + \hat{k}_y^2)} & 0 & 0 \end{pmatrix}$$

FIG. 2: Mode-resolved evolution matrix \mathcal{A}_m obtained from the Fourier-sum representation of the initial parallel vector potential $\hat{A}_{\parallel,0} = a_0 \cos(mx)$. Using the sifting property of the Dirac delta distribution, the convolution reduces to an algebraic eigensystem for each mode number m . The spectrum of \mathcal{A}_m is analyzed as a function of β , k_x , and \hat{k}_y , allowing investigation of the condition number and pseudospectral behavior near marginal stability.

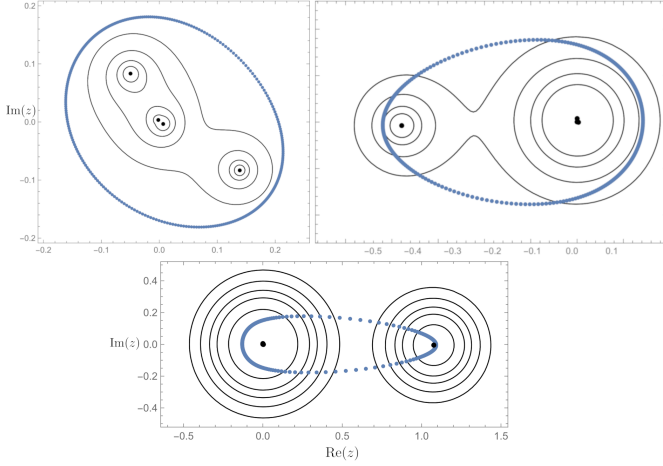


FIG. 3: Contour plots of the ε -pseudospectrum of \mathcal{A}_m , overlaid with the numerical abscissa (blue dotted line), for $m = 1$ and $\hat{k}_y = 0.1, 1, 10$ (left, right, bottom). When $\hat{k}_y \geq 1$, the spectrum becomes purely real and shifts progressively toward the unstable half-plane.

We conclude that the governing operator exhibits very large condition numbers and is therefore strongly non-normal. This non-normality renders transient growth a natural feature of the system dynamics and provides a plausible mechanism for “explosive” magnetic reconnection, which is characterized by transient phases in which an initial linear growth is followed by a rapid, superlinear amplification^{24,26,27,59–61}.

C. Tearing Instability and explosive Magnetic Reconnection

We now present simulations of a tearing unstable Harris-Sheet⁶²

$$\hat{A}_{\parallel} = \beta \cdot \left(\frac{A_0}{\cosh(\eta \cdot 4\pi \hat{x}/L_{\hat{x}})^2} + A_1 \cdot \cos(m_y \cdot 2\pi \hat{y}/L_{\hat{y}}) \right) \cos(\pi \hat{x}/L_{\hat{x}}) \quad (46)$$

$$\hat{u}_e = \frac{1}{N_0 \cdot \beta} \Delta \hat{A}_{\parallel} \quad (47)$$

with the parameters: sheet amplitude := A_0 , perturbation amplitude := A_1 , perturbation mode number := m_y , background density := N_0 , sheet width := η . To capture all X-points, one can make use of the relative global partition reconnection rate⁶³

$$\gamma_{glob} = \frac{d}{dt} \ln \left(\sum_{x_p} \delta \hat{A}_{\parallel}(x_p) \right) = \frac{d}{dt} \ln \left(\sum_{x_p} |\hat{A}_{\parallel}(\vec{x}_p, \hat{t}) - \hat{A}_{\parallel,eq}(\vec{x}_p)| \right)$$

where all the X-points are located by finding local minima and tracking their evolution. This method depends on the choice of $\hat{A}_{\parallel,eq}$, which is defined by the unperturbed current sheet eq. 46. In a numerical study however, it is suboptimal to compare discrete results with several layers of (subroutine) boundary conditions to an analytical function. We hence choose the $\hat{k}_y = 0$ mode of \hat{A}_{\parallel} to be the equilibrium. The differences in the obtained rate depend on the k_x spectrum and will slightly differ from the unperturbed initial condition³⁸.

Figure 4 shows a typical reconnection event, for a marginally stable Harris-sheet configurations, with multiple phases, including a linear phase, and an explosive event, finalizing the topological change. For comparability we present the obtained growth rates in units of the Alfvén velocity $\gamma_{eff} = \hat{\gamma}_{num}/(v_A B_0)$. The growth rate increases from $\gamma_{eff} \sim 0.1 v_A B_0$ in the linear phase to a peak of $\gamma_{eff} \sim 0.2 v_A B_0$ during explosive reconnection, which is consistent with previous observations

In the $m = 1$ case the reconnection happens via a single X-point making it easy to distinguish different phases in the evolution. For $\hat{d}_e \geq 0.5$, the obtained growth rates decrease, and generally show a phase of exponential growth. The presence of a linear phase is especially visible in a logarithmic plot of the time evolution of $\Delta \Psi = |\hat{A}_{\parallel}(\vec{x}, \hat{t}) - \hat{A}_{\parallel}(\vec{x}_0, 0)|$, presented in figure 5 (left).

Finally, the growth rate is investigated in the regime that fits the analytical estimate, where the small stability parameter approximation $\Delta' \ll 1$ ($m = 4.9$) was used multiple times, in the range $\hat{d}_e \sim 1$, $\tau_i \in \{0, 1\}$. This regime is commonly referred to as the marginally stable regime and is therefore borderline stable, being achieved by the choice of an appropriate \hat{k}_y close to, but smaller than, 1. The linear phases of a current sheet perturbed with $m = 1$, for which the analytical estimate is not valid, are further compared in various regimes, includ-

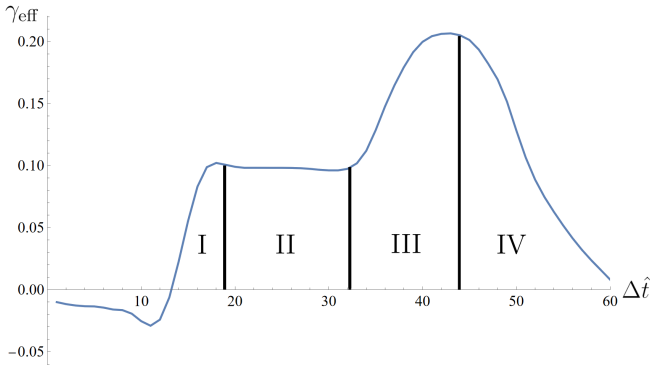


FIG. 4: Explosive magnetic reconnection for a warm $\tau_i = 1$ Harris-sheet at $\beta = 5 \cdot 10^{-3}$ and $m = 1$. The initial phase is followed by a hyper-linear (I), linear (II), and again hyper-linear (III) (explosive) phase until the reconnection is complete (IV). The linear phase grows around $\gamma = 0.1v_A B_0$ while the explosive reconnection peaks at $\gamma \approx 0.2v_A B_0$.

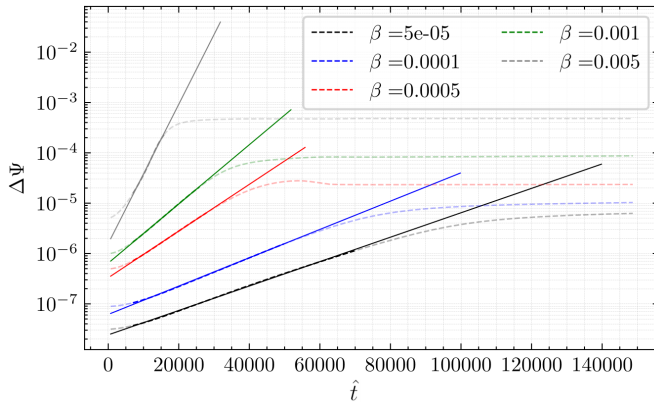


FIG. 5: Logarithmic plot of the time evolution of $\Delta\Psi$ for different values of β . As expected from the dispersion relation, the change in $\Delta\Psi$ decreases with β and the reconnection shows a clear linear phase (straight line).

ing arbitrary wavelength and long-wavelength-approximated (LWL) polarization at $L_x = L_y = 32\rho_s$, $n_x = n_y = 1024$, and $\nu = 10^{-8}$. In Fig. 6, the numerically obtained growth rates of the linear phase are compared with the analytical estimate for various parameters. While good agreement with the analytical estimate is observed in the marginally stable case, deviations are found when $\hat{d}_e = d_e/\rho_s \sim 1$ and $m = 1$. This case is also compared with results obtained from the open-source gyrofluid code FELTOR⁶⁴. As expected, FLR effects are generally found to play a minor role in most cases, especially when the polarization equation is used in long-wavelength-approximated form. However, sensitivity to approximations in the polarization equation is observed for the $m = 1$ perturbed system, as the deviation from the analytical estimate appears to be corrected when low hyperviscosity $\nu \sim 10^{-8}$ is applied. It is noted that the analytical estimate was derived in the cold-ion limit $\tau_i = 0$.

Figure 7 shows a comparison of the Arakawa discretization with $\nu = 10^{-7}$ and an upwind scheme applied to the OB-approximated and arbitrary-wavelength polarization models. The latter discretization introduces a dissipation on its own⁶⁵. The color contours represent the parallel current density \hat{J}_{\parallel} , illustrating the formation and nonlinear evolution of the reconnecting current sheet. Both discretization schemes produce qualitatively and quantitatively similar current structures, indicating that the centered Arakawa scheme with weak hyperdiffusion provides sufficient regularization without introducing significant numerical artifacts. Moreover, the comparison highlights that reconnection proceeds more rapidly when the NOB polarization is employed, consistent with the enhanced dynamical response in that model. Overall, the agreement between the Arakawa and upwind results confirms that the observed acceleration of reconnection is a physical effect rather than a consequence of the numerical scheme.

Figure 8 shows the time evolution of the normalized \hat{k}_y spectrum of a marginally stable $m = 4.9$ and unstable $m = 1$ current sheet. The marginally stable $m = 4.9$ mode persists until reconnection is triggered through the excitation of lower mode numbers. Its harmonics are present but are expected to remain linearly stable. In contrast, in the $m = 1$ case, reconnection is driven directly by the initial perturbation and occurs significantly earlier than in the marginally stable scenario.

Note that the marginally unstable cases (figure 6) decay after significant rearrangement of the initially excited mode. The obtained reconnection rate is intermittent, as multiple X-points emerge and vanish, and the final reconnection event can be described as "explosive".

To investigate the time evolution of the current sheet and possible FLR effects, x -cuts of several quantities are plotted and compared at different times with results presented in the literature^{25,38}. Figure 9 shows slices of $\delta\hat{A}_{\parallel}$ at the time when the x -point emerges, and changes in the indent of \hat{A}_{\parallel} due to ion FLR effects are observed, similar to those reported in Ref^[25], together with narrowing of the current sheet and island formation. However, at this stage of the reconnection, a larger island width is observed when ion temperature effects are included, and the electric potential is found to display the expected multipolar structure. In addition, the typical left/right asymmetry in the potential $\hat{\phi}_e$ and in \hat{J}_{\parallel} is observed.

When the reconnection is almost completed and possible elongation of the reconnection zone is fully developed, the indent in \hat{A}_{\parallel} has nearly vanished as constant behavior is approached. The electric potential then becomes rather chaotic with increased fine structure in the warm ion $\tau_i = 1$ case, which translates via N_Z to more fine structure in the current \hat{J}_{\parallel} .

IV. PLASMOID FORMATION AND ASPECT RATIO EFFECTS

To further test the Full- F framework of the code, a situation is constructed in which the initial current \hat{J} is mainly carried

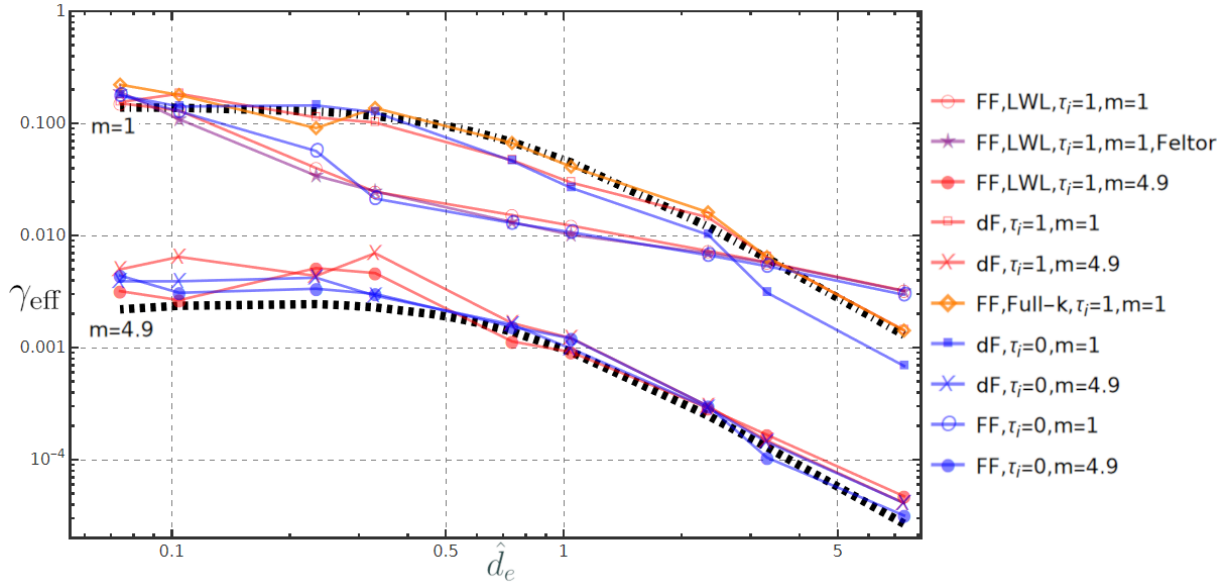


FIG. 6: Analytical estimates $\hat{\gamma}_{in}$ (black dotted and dot-dashed lines) for marginal stability $m = 4.9$, $m = 1$ and obtained reconnection rates $\hat{\gamma}$ for multiple parameters, δF and $Full - F$ models. The general trend for the analytical estimate is recovered, and the obtained linear growth rates fit the analytical estimate well. As expected, in the square box, FLR effects play a minor role and affect the reconnection rate only marginally in most cases. In the $m = 1$ case, the values deviate when $\hat{d}_e = d_e/\rho_s \sim 1$ and only converges back to the analytical estimate when the arbitrary wavelength polarization equation (Full-k) is used in combination with low hyperviscosity of $\nu \propto 10^{-8}$.

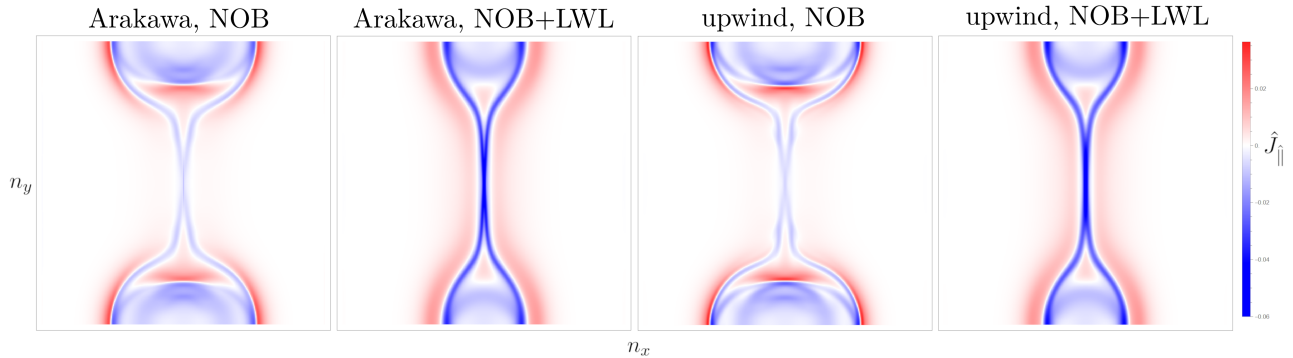


FIG. 7: Comparison of the Arakawa discretization with $\nu = 10^{-7}$ and upwind-scheme for OB-approximated and arbitrary wavelength polarization. Both schemes yield similar results, and the reconnection is accelerated when NOB polarization is used.

by the ions,

$$-\frac{1}{\beta} \hat{\nabla}_{\perp}^2 \hat{A}_{\parallel} = \hat{\Gamma}_1(\hat{U}_i),$$

as shown in Fig. 10. In this regime, not only a disparity in the current evolution due to μ_e is expected, but the ion contribution in the polarization equation also becomes relevant when the gyrocenter density amplitudes deviate significantly from the initial (or mean) value N_0 . Owing to the low electron inertia, a significant electron current is formed as a response, thereby contributing to the reconnection process. The resulting configuration exhibits plasmoid formation with intermedi-

ate x -points, which contribute to the total growth rate. Nevertheless, the obtained growth rate is found to be hardly comparable with the case in which the electron current is used for the initialisation, and the growth rates are generally smaller by a factor of 10 for all values of β .

In the regime with significant ion contribution, corresponding FLR effects are also expected to play a role in the reconnection. The parallel current \hat{J}_{\parallel} for a square box (aspect ratio 1) with $\beta = 10^{-4}$, $\mu_e = \mu_{e,p}$, and warm ions with $\tau_i = 1$. The typical quadrupolar configuration of the electric potential is formed in response to the reconnection, leading to stabilisation and ultimately elongation of the reconnection zone⁶⁶.

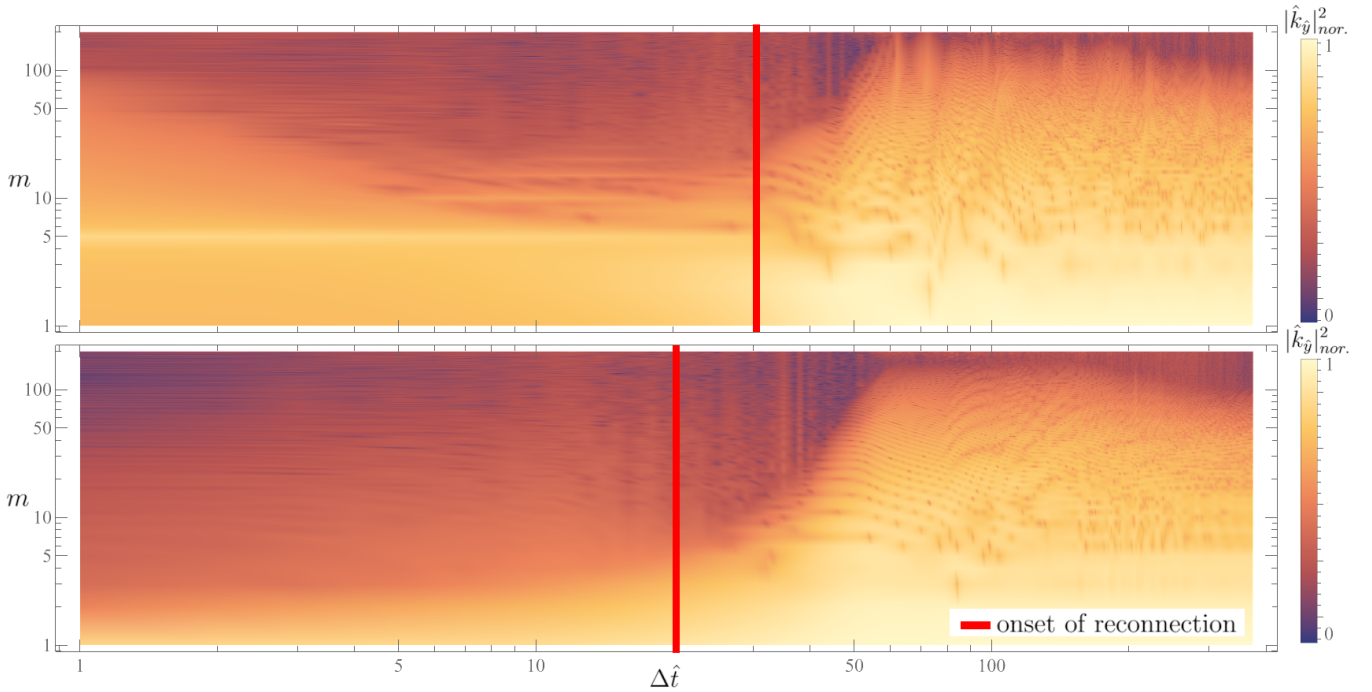


FIG. 8: Time evolution of the normalized \hat{k}_y spectrum (excluding the stable $\hat{k}_y = 0$ mode) for a marginally stable (top) and an unstable sheet with $m = 1$ (bottom) perturbation. The marginally stable $m = 4.9$ mode survives until the reconnection takes place via excitation of lower mode numbers, its harmonics are visible but are linearly stable. The $m = 1$ case reconnection occurs via the initial perturbation and happens significantly earlier than in the marginally stable case.

When the same system is simulated with an aspect ratio of 2, plasmoid growth is expected, and, as shown in Fig. 11 and 12, this is indeed observed. In this case, a competing tearing mode grows stronger than the initial $m = 1$ perturbation, resulting in a plasmoid instability for two regimes of \hat{d}_e .

To investigate the general behavior with respect to the aspect ratio, a Full- F system is considered that is perturbed with $m = 1$ and $\tau_i = 1$, and aspect ratios of up to 16 are examined. Figure 13 shows an increase in the number of plasmoids with increasing aspect ratio. From an aspect ratio of 8 onwards, reconnection of the current is observed to occur through large plasmoids that are of the order of the main islands. In these configurations, the phases of reconnection are found to vary strongly between the multiple x -points, such that reconnection may already be completed at some locations while being simultaneously in an early stage at others. At very high aspect ratios, multiple regions with small stochastic islands are observed around the main islands.

V. CONCLUSION AND SUMMARY

We have investigated collisionless magnetic reconnection and plasmoid formation in a two-dimensional Full- F gy-

rofluid framework designed for fusion-relevant, strongly magnetized and low- β regimes. Using the recently developed GREENY code³⁴, we quantified tearing-mode growth, transient (non-modal) amplification and explosive reconnection, and mapped the onset and morphology of plasmoid dynamics as functions of electron inertia, ion FLR effects, polarization modeling, and system aspect ratio.

A main outcome is that the Full- F gyrofluid model reproduces key signatures of fast collisionless reconnection reported in Hall-MHD, gyrokinetic, and kinetic simulations, with peak normalized rates of order $0.1\text{--}0.2v_A B_0$ in the parameter range studied^{29,30,32,33}. In the marginally stable regime, numerically measured linear growth rates agree well with analytical tearing-mode estimates when arbitrary-wavelength polarization is retained, whereas long-wavelength and Oberbeck–Boussinesq polarization approximations can introduce noticeable deviations at small β and intermediate \hat{d}_e . This demonstrates that consistent polarization physics is essential for quantitative reconnection studies at ρ_s scales.

The linearized Full- F system is shown to be strongly non-normal. Large condition numbers, a positive numerical abscissa, and ε -pseudospectra extending into the unstable half-plane indicate that transient amplification is intrinsic to the dynamics. This provides a coherent explanation for the commonly observed transition from an initial linear tearing phase to a short-lived phase of enhanced reconnection (“explosive” behavior), and rationalizes intermittent reconnection in configurations where the modal growth rate alone would suggest

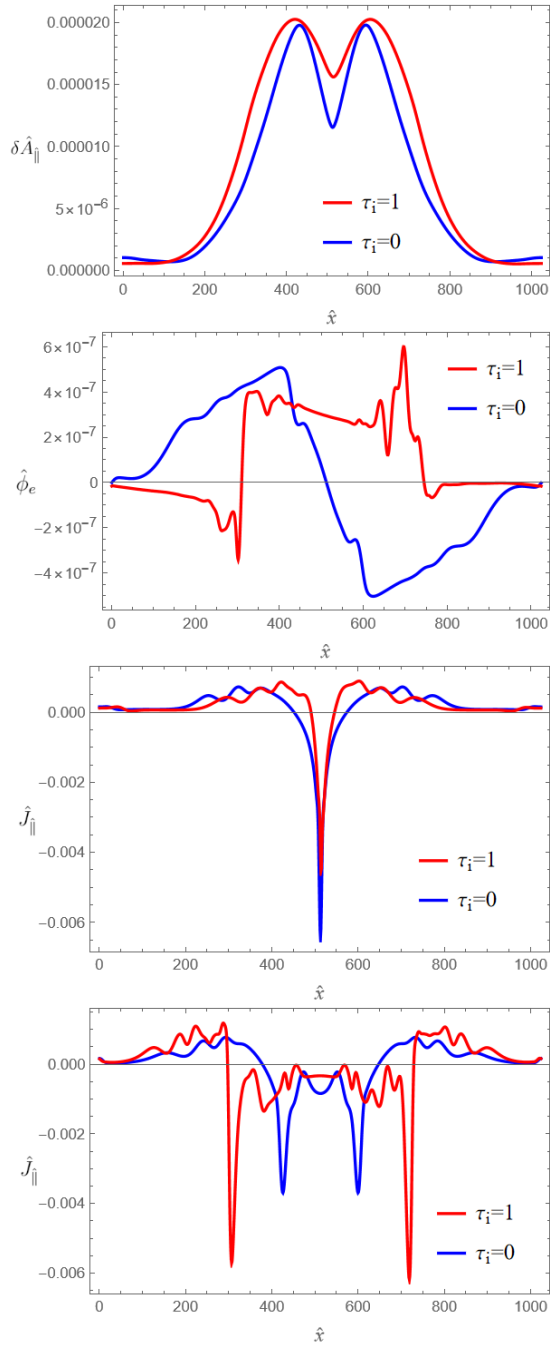


FIG. 9: 1D slices of fields in x -direction at the beginning of the magnetic reconnection, when the X-point is formed. Although the observed reconnection rates are often similar, the time evolution of the exact quantities differs, including an asymmetry in the potential $\hat{\phi}_e$ and \hat{J}_{\parallel} .

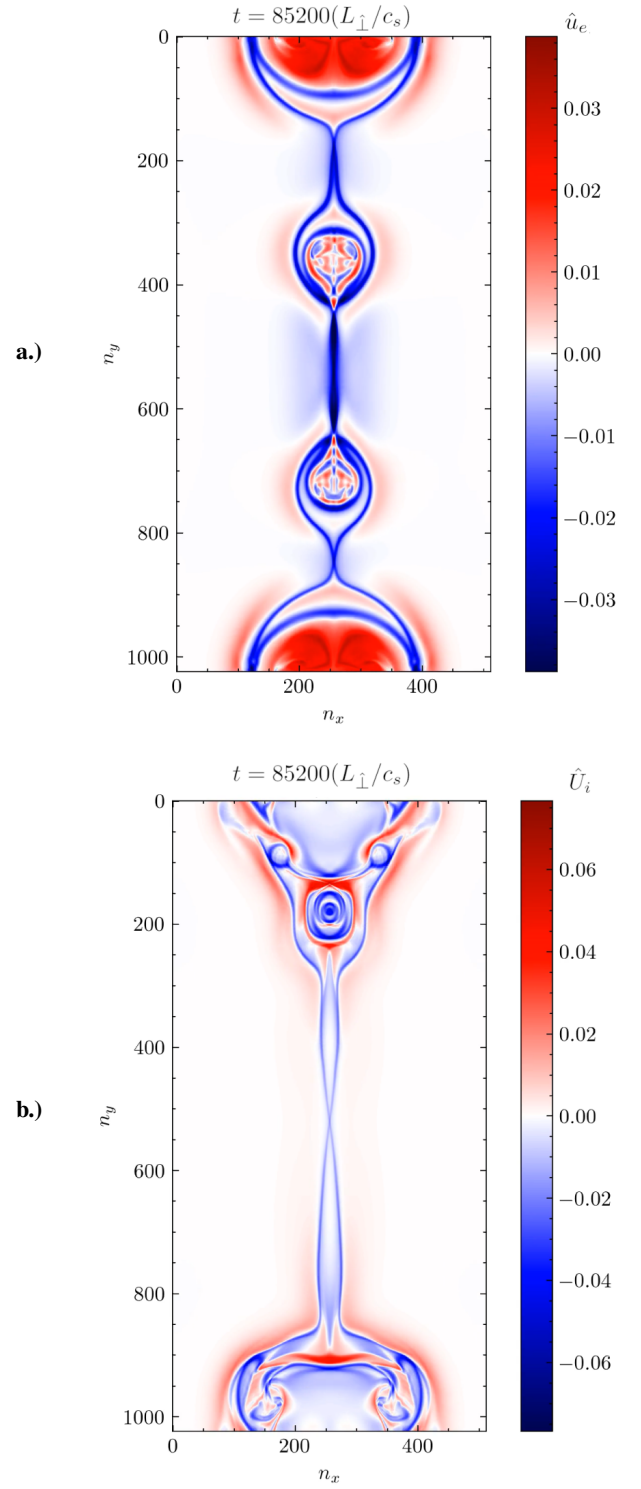


FIG. 10: Parallel velocities $\hat{U}_z(\hat{x})$ for an ion-current induced magnetic reconnection event with aspect ratio $\frac{L_y}{L_x} = 2$ and $\tau_i = 1$. The electron current shows two plasmoids growing, while there are no plasmoids developed in the ion current at this time of the reconnection.

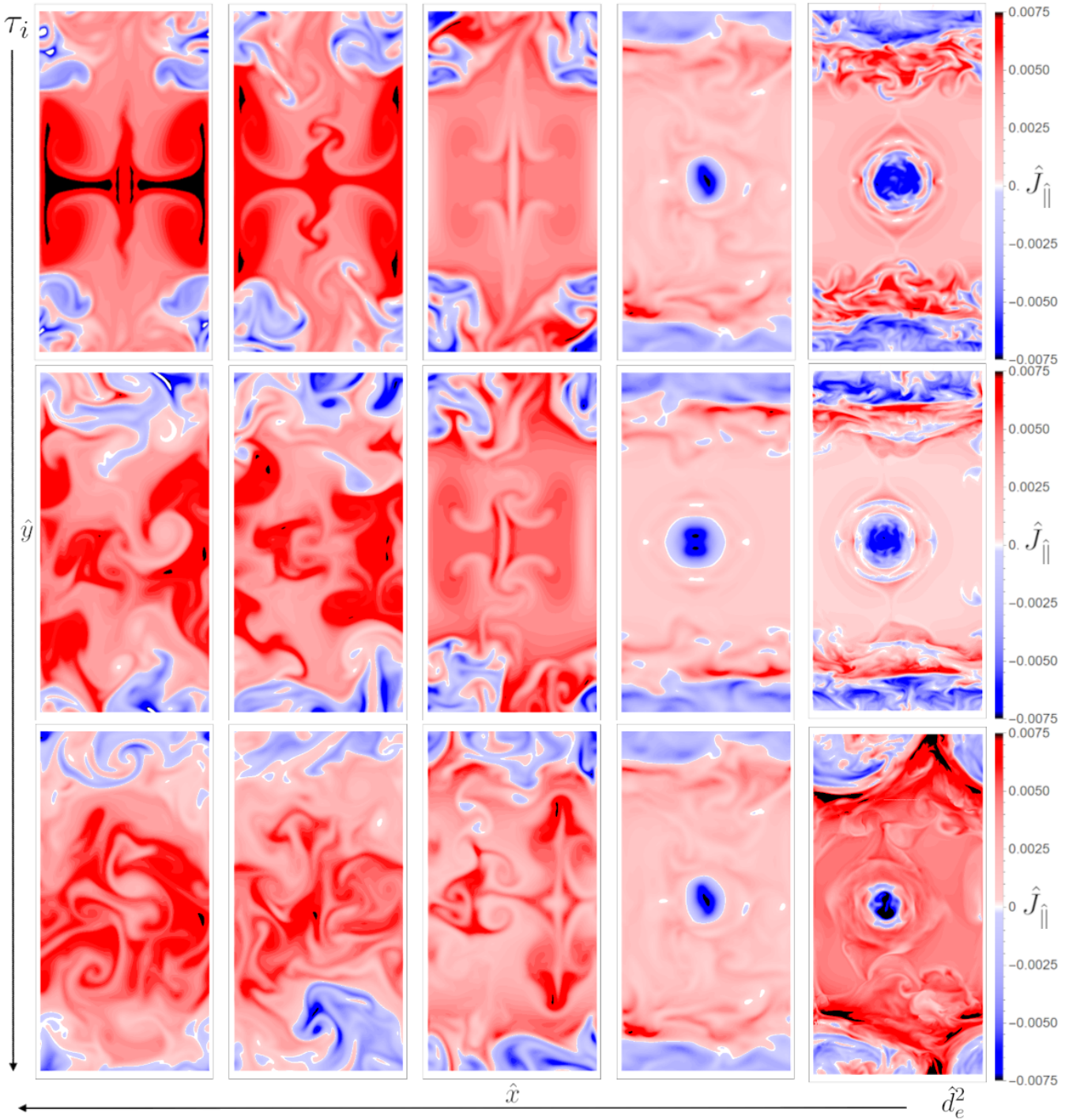


FIG. 11: Ion-current sheet with aspect ratio 2 and (left to right) $\tau_i \in \{0, 1, 5\}$ and $\hat{d}_e \in \{5446.62, 544.662, 54.4662, 5.44662, 0.544662\}$. With increasing ion temperature, the reconnection becomes turbulent but the number of plasmoids is not affected.

only weak instability.

Ion FLR effects are found to be secondary for linear growth rates in square domains, but they influence current-sheet morphology, island width, and the fine structure of the reconnection region in warm-ion regimes, consistent with earlier gyrofluid and reduced-kinetic studies^{25,27}. In particular, when

a significant fraction of the equilibrium current is carried by ions, FLR effects contribute to the shaping of the reconnection geometry and can facilitate plasmoid formation in elongated systems through enhanced species disparity and nonlinear coupling.

A systematic scan in aspect ratio shows that plasmoid for-

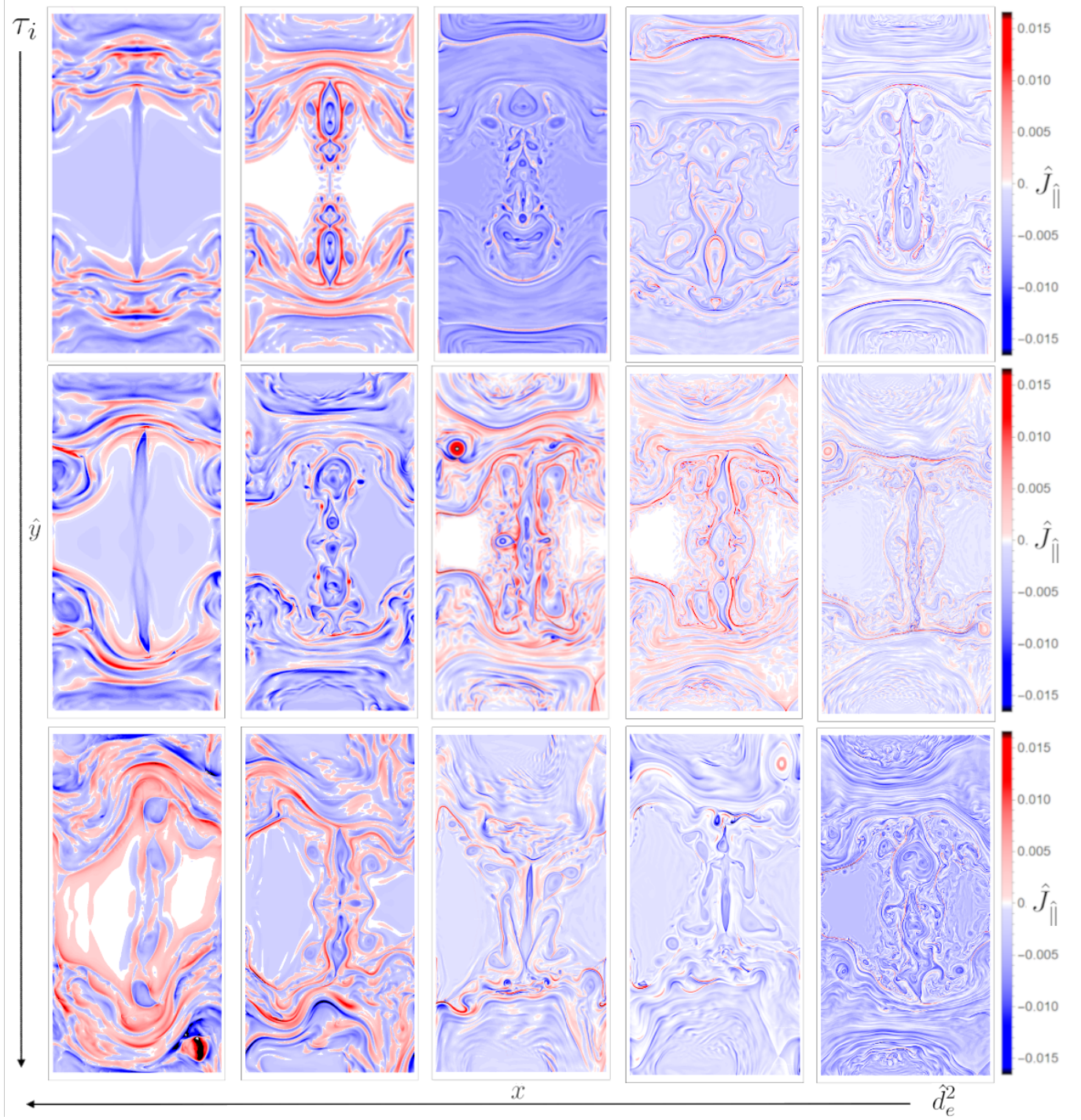


FIG. 12: Ion-current sheet with aspect ratio 2 and (left to right) $\tau_i \in \{0, 1, 5\}$ and $\hat{d}_e^2 \in \{0.0544662, 0.00544662, 5.44662 \times 10^{-4}, 5.44662 \times 10^{-5}, 5.44662 \times 10^{-6}\}$. With increasing ion temperature, the reconnection becomes turbulent but the number of plasmoids is not affected.

mation is strongly promoted in elongated current sheets. With increasing $L_{\hat{y}}/L_{\hat{x}}$, multiple plasmoids emerge and dominate the nonlinear dynamics, yielding a hierarchy of x -points and magnetic islands and a spatially inhomogeneous, intermittent reconnection process, in qualitative agreement with plasmoid theory and previous numerical studies^{8,67}. At sufficiently

large aspect ratios, reconnection proceeds through coexisting large islands and surrounding smaller stochastic structures, indicating a transition toward a multiscale reconnection regime.

Numerically, we emphasize that centered differencing requires explicit regularization. In our implementation this is achieved via a weak hyperdiffusion term, chosen small

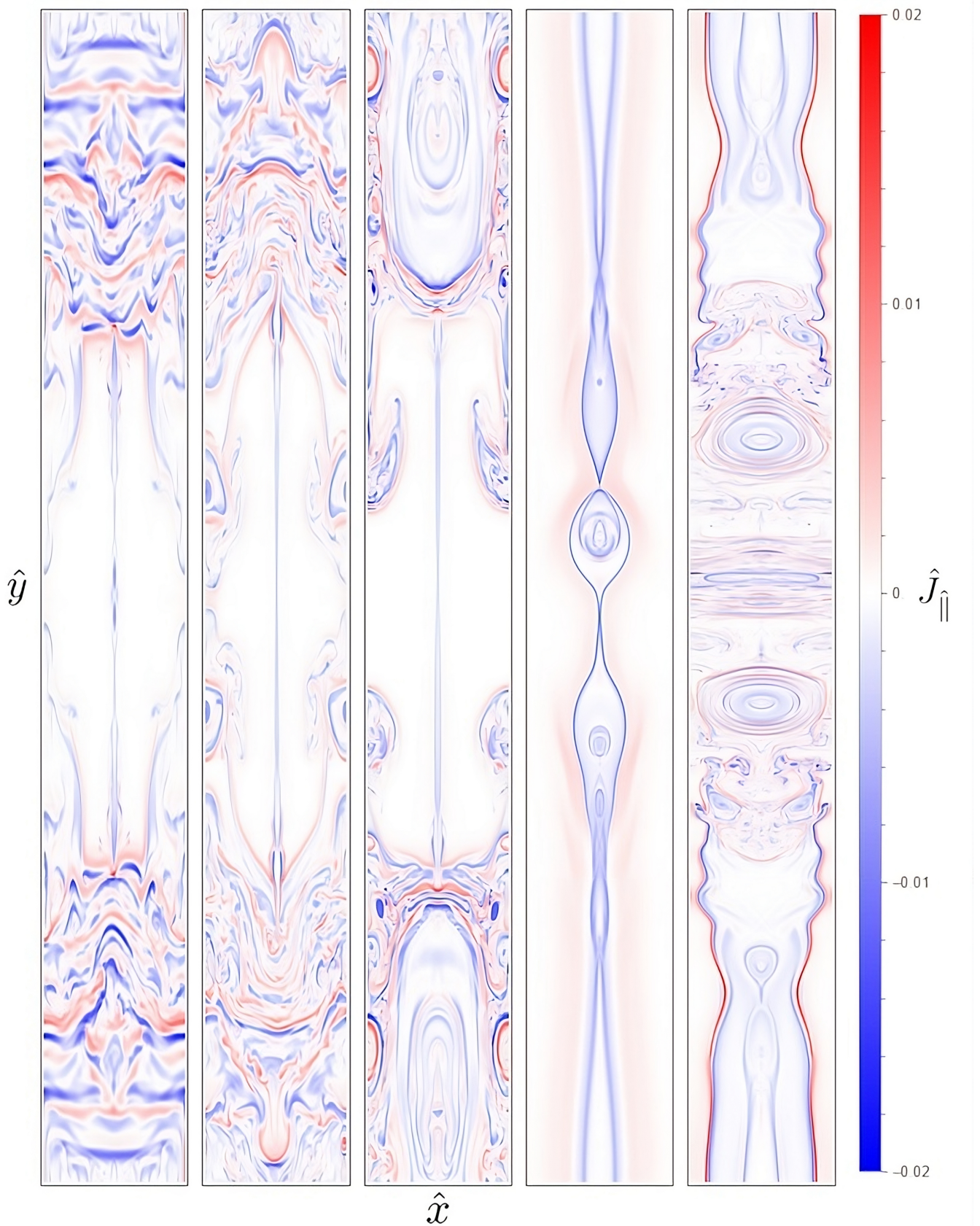


FIG. 13: Full- F ion-current induced Harris-sheet with aspect ratios from (left to right) $r \in \{2, 3, 4, 8, 16\}$ and $\tau_i = 1$ and LWI polarization. The number and size of plasmoids scales with the aspect ratio, and very high aspect ratio yields large islands surrounded by a stochastic "small" island region.

enough to avoid artificially broadening the reconnecting current sheet while still suppressing grid-scale noise. Importantly, Fig. 7 demonstrates that an Arakawa discretization with $\nu = 10^{-7}$ and an upwind scheme yield very similar parallel-current structures for both OB-approximated and arbitrary-wavelength polarization models, while reconnection is consistently accelerated when NOB (arbitrary-wavelength) polarization is employed. This comparison supports two key conclusions: (i) the qualitative and quantitative reconnection dynamics reported here are not artifacts of the discretization choice, and (ii) the reconnection acceleration observed with NOB polarization reflects a physical model difference rather than numerical bias.

Finally, while convergence is robust for long-wavelength polarization at moderate resolution, arbitrary-wavelength polarization introduces ρ_s -scale structure whose detailed origin and sensitivity to numerical dissipation merit further investigation. Future work should therefore include systematic dissipation-parameter scans, improved iterative solvers for polarization/Ampère closures, and extensions toward three-dimensional coupling (e.g. shear-Alfvénic dynamics) and reconnection in the presence of drift-wave turbulence. Overall, the present results establish Full- F gyrofluid modeling as a quantitatively consistent and computationally efficient framework for studying fast reconnection, transient amplification, and plasmoid dynamics in tokamak-relevant parameter regimes.

ACKNOWLEDGMENTS

This work has been carried out within the framework of the EUROfusion Consortium, funded by the European Union via the Euratom Research and Training Programme (Grant Agreement No 101052200 — EUROfusion). Views and opinions expressed are however those of the author(s) only and do not necessarily reflect those of the European Union or the European Commission. Neither the European Union nor the European Commission can be held responsible for them.

The author thanks Bruce Scott and Matthias Wiesenberger (DTU) for valuable discussions.

A. Author Contributions

F. F. Locker: Data Curation (lead); Conceptualization (equal); Validation (equal); Software (equal); Visualization (equal); Writing - original draft (lead); Methodology (equal); Formal analysis (lead); Project Administration (equal); **M. Rinner:** Validation (supporting); Visualization (equal); Software (supporting); **M. Held:** Conceptualization (equal); Methodology (equal); **A. Kendl:** Supervision (lead); Conceptualization (equal); Writing - review & editing (equal); Resources (lead); Project Administration (equal);

DATA AVAILABILITY STATEMENT

The full code is available on <https://git.uibk.ac.at/c7441315/greeny> and the presented data that supports the findings of this study are available from the corresponding author upon reasonable request.

Appendix A: Derivation of the Dispersion Relation

After neglecting second order terms, we find the linearised system of equations

$$i \frac{g}{\beta} \tilde{n}_e = -a'_{\parallel, \text{eq}} \left(\frac{A_0}{N_0} a''_{\parallel, \text{eq}} \tilde{n}_e + N_0 \tilde{U}_e \right) + a'''_{\parallel, \text{eq}} \tilde{A}_{\parallel}, \quad (1^L)$$

$$i \frac{g}{\beta} \tilde{N}_i = -a'_{\parallel, \text{eq}} N_0 \tilde{U}_i, \quad (2^L)$$

$$i \frac{g}{\beta} \left(\tilde{U}_e + \frac{1}{\mu_e} \beta \tilde{A}_{\parallel} \right) = - \left(\frac{1}{\beta N_0} a'''_{\parallel, \text{eq}} + \frac{1}{\mu_e} a'_{\parallel, \text{eq}} \right) \tilde{\phi} + \frac{1}{\mu_e N_0} a'_{\parallel, \text{eq}} \tilde{n}_e - \frac{A_0}{N_0} a''_{\parallel, \text{eq}} \left(a'_{\parallel, \text{eq}} \tilde{U}_e - \frac{1}{N_0} a'''_{\parallel, \text{eq}} \tilde{A}_{\parallel} \right), \quad (3^L)$$

$$\frac{i}{\beta} g \left(\tilde{U}_i + \beta \tilde{A}_{\parallel} \right) = -a'_{\parallel, \text{eq}} \tilde{\phi}, \quad (4^L)$$

$$- \left(\tilde{A}_{\parallel}'' - k^2 \tilde{A}_{\parallel} \right) = N_0 \left(\tilde{U}_i - \tilde{U}_e \right) - \frac{A_0}{N_0} a''_{\parallel, \text{eq}} \tilde{n}_e, \quad (5^L)$$

$$- \left(\tilde{\phi}'' - k^2 \tilde{\phi} \right) = \frac{1}{N_0} \left(\tilde{N}_i - \tilde{n}_e \right). \quad (6^L)$$

where we introduced the quantity $g := \frac{\gamma}{k A_0}$. From this set one can derive another equation by subtracting equation (1^L) from (2^L) and substituting the $(\tilde{U}_i - \tilde{U}_e)$ term with equation (5^L) and the $(\tilde{N}_i - \tilde{n}_e)$ term with equation (6^L). Conducting this, one gets

$$i g N_0 \left(\tilde{\phi}'' - k^2 \tilde{\phi} \right) - a'''_{\parallel, \text{eq}} \beta \tilde{A}_{\parallel} + a'_{\parallel, \text{eq}} \left(\beta \tilde{A}_{\parallel}'' - k^2 \beta \tilde{A}_{\parallel} \right) = 0. \quad (7^L)$$

This last equation is very fundamental and found as an intermediate result in many other derivations of the tearing instability parameter^{44,68}.

1. Solving for different Regimes

Solving this system of equations for \tilde{A}_{\parallel} and $\tilde{\phi}$ we use the ordering

$$\Delta' d_e \ll 1, \quad \gamma \ll 1, \quad d_e^2 \ll 1,$$

to obtain an analytically solvable differential equation. Substitutions, rearrangements and simplifications were done by pen and paper and double checked with the CAS Wolfram

Mathematica.⁵⁷ For small growth rates γ we can decouple ϕ and \tilde{A}_{\parallel} in equation 7^L and obtain

$$-a'''_{\parallel,\text{eq}}\tilde{A}_{\parallel} + a'_{\parallel,\text{eq}}(\tilde{A}''_{\parallel} - k^2\tilde{A}_{\parallel}) = 0. \quad (\text{A1})$$

which is a Legendre differential equation. Note that neglecting γ terms holds only because g becomes independent of β beforehand. Otherwise that would not universally hold as $\beta \ll 1$ too. With

$$\begin{aligned} a'_{\parallel,\text{eq}} &= -\tanh(x) \\ \text{and} \quad a'''_{\parallel,\text{eq}} &= 2 \frac{\tanh(x)}{\cosh^2(x)} \end{aligned}$$

The solution is

$$\tilde{A}_{\parallel,\text{out}} = \tilde{A}_{\parallel,0} \begin{cases} e^{-kx} (1 + \tanh(x)/k), & x > 0 \\ e^{kx} (1 - \tanh(x)/k), & x < 0 \end{cases}, \quad (\text{A2})$$

where $\tilde{A}_{\parallel,0} \in \mathbb{R}$ is an arbitrary constant.

The function has a discontinuous derivative at $x = 0$, just as it is needed for the tearing stability parameter Δ' , which is defined by the solution of this outermost region

$$\Delta'_{outer} = \lim_{x \rightarrow 0^+} \frac{\tilde{A}'_{\parallel,\text{out}}}{\tilde{A}_{\parallel,\text{out}}} - \lim_{x \rightarrow 0^-} \frac{\tilde{A}'_{\parallel,\text{out}}}{\tilde{A}_{\parallel,\text{out}}} = 2 \left(\frac{1}{k} - k \right). \quad (\text{A3})$$

For small x one can linearize the above solution. Near the resonant surface at $x = 0$ the outer solution behaves like

$$\tilde{A}_{\parallel,\text{out}}(x) \approx \tilde{A}_{\parallel,0} \left(1 + \frac{\Delta'}{2} |x| \right).$$

Lets now solve the equations for the so called "inner region" close to the current sheet, so for $|x| \ll 1$.

By Taylor-expanding the used equilibrium function $a_{\parallel,\text{eq}}(x) = -\ln(\cosh(x))$ one finds

$$\begin{aligned} a_{\parallel,\text{eq}}(x) &\approx 0, & a'_{\parallel,\text{eq}}(x) &\approx -x, \\ a''_{\parallel,\text{eq}}(x) &\approx -1, & a'''_{\parallel,\text{eq}}(x) &\approx 2x. \end{aligned}$$

Since all k^2 terms originate from a y derivative, ($k = \hat{k}_y$), and the variations of the functions are larger in x -direction, the following can be applied

$$\begin{aligned} k^2 \tilde{\phi} &\ll \tilde{\phi}'' , \\ k^2 \tilde{A}_{\parallel} &\ll \tilde{A}''_{\parallel} , \\ (k^2 - 2) \tilde{A}_{\parallel} &\ll \tilde{A}''_{\parallel} , \end{aligned}$$

With these approximations the equations (1^L) to (7^L) be-

come

$$\left(i \frac{g}{\beta} + \frac{A_0}{N_0} x \right) \tilde{n}_e = N_0 x \tilde{U}_e + 2x \tilde{A}_{\parallel}, \quad (1^x)$$

$$i \frac{g}{\beta} \tilde{N}_i = N_0 x \tilde{U}_i, \quad (2^x)$$

$$\begin{aligned} \left(i \frac{g}{\beta} + \frac{A_0}{N_0} x \right) \tilde{U}_e &= - \left(i g \frac{1}{\mu_e} + \frac{A_0}{N_0} \frac{2}{N_0} x \right) \tilde{A}_{\parallel} \\ &\quad - x \left(\frac{2}{\beta N_0} - \frac{1}{\mu_e} \right) \tilde{\phi} - \frac{1}{\mu_e N_0} x \tilde{n}_e, \end{aligned} \quad (3^x)$$

$$i \frac{g}{\beta} \tilde{U}_i = -i g \tilde{A}_{\parallel} + x \tilde{\phi}, \quad (4^x)$$

$$-\tilde{A}''_{\parallel} = N_0 (\tilde{U}_i - \tilde{U}_e) + \frac{A_0}{N_0} \tilde{n}_e, \quad (5^x)$$

$$-\tilde{\phi}'' = \frac{1}{N_0} (\tilde{N}_i - \tilde{n}_e), \quad (6^x)$$

$$0 = g \tilde{\phi}'' + i \frac{x}{N_0} \beta \tilde{A}''_{\parallel}. \quad (7^x)$$

We now want to find a ODE for \tilde{A}_{\parallel} . For that we start with 7^x and eliminate $\tilde{\phi}''$ to obtain

$$g(n_e - N_i) = \beta i x \tilde{A}''_{\parallel}.$$

Then one has to insert for n_e (eliminate U_e in the electron density equation first), U_i and N_i to get

$$\begin{aligned} \tilde{A}''_{\parallel} &= -\tilde{A}_{\parallel} \beta N_0 - \frac{i \beta N_0 \phi x}{g} + \frac{2 \tilde{A}_{\parallel} g^2 \mu_e N_0^2}{\Omega} - \\ &\quad - \frac{\tilde{A}_{\parallel} \beta^2 g^2 N_0^3}{\Omega} + \frac{2 i g \mu_e N_0^2 \phi x}{\Omega} - \frac{i \beta g N_0^3 \phi x}{\Omega} \end{aligned}$$

where $\Omega = -g^2 \mu_e N_0^2 + 2i A_0 \beta g \mu_e N_0 x + \beta^2 (A_0^2 \mu_e + N_0^2) x^2$ is used to shorten it. We can rearrange that to

$$\tilde{A}''_{\parallel} + N_0 \frac{[\Omega \beta + g^2 N_0 (\beta N_0 - 2 \mu_e)] (\tilde{A}_{\parallel} g + i \phi x)}{g \Omega} = 0.$$

The complex part of $Im[\Omega] = 2A_0 \beta g \mu_e N_0 x$ is relatively small and can be neglected. This can be cast into the form of

$$\tilde{A}''_{\parallel} = \kappa \left(\tilde{A}_{\parallel} + \frac{i \tilde{\phi} x}{g} \right) \quad (\text{A4})$$

where κ is now

$$\kappa = \frac{N_0 (g^2 N_0 (\beta N_0 - \mu_e (2 + \beta N_0)) + \beta^3 (A_0^2 \mu_e + N_0^2) x^2)}{-g^2 \mu_e N_0^2 + \beta^2 (A_0^2 \mu_e + N_0^2) x^2}. \quad (\text{A5})$$

The small Δ' hypothesis allows one to set $\tilde{A}_{\parallel,\text{in}}$ approximately constant around the resonant surface $x = 0$ (constant- $\tilde{A}_{\parallel,\text{in}}$ approximation), thus to apply this one sets $\tilde{A}_{\parallel,\text{in}}(x) = \tilde{A}_{\parallel,\text{in},0} + \tilde{A}_{\parallel,\text{in},1}(x)$ with $|\tilde{A}_{\parallel,\text{in},1}| \ll \tilde{A}_{\parallel,\text{in},0}$. Inserting this into relation

A4 yields

$$\frac{1}{\kappa} (\tilde{A}_{\parallel, \text{in}, 0} + \tilde{A}_{\parallel, \text{in}, 1})'' = (\tilde{A}_{\parallel, \text{in}, 0} + \tilde{A}_{\parallel, \text{in}, 1}) + i \frac{x}{g} \tilde{\phi} \quad (\text{A6})$$

$$\Leftrightarrow \quad (\text{A7})$$

$$\frac{1}{\kappa} \tilde{A}_{\parallel, \text{in}, 1}'' = \tilde{A}_{\parallel, \text{in}, 0} \left(1 + \frac{\tilde{A}_{\parallel, \text{in}, 1}}{\tilde{A}_{\parallel, \text{in}, 0}} \right) + i \frac{x}{g} \tilde{\phi} \quad (\text{A8})$$

$$\Rightarrow \quad \frac{1}{\kappa} \tilde{A}_{\parallel, \text{in}, 1}'' = \tilde{A}_{\parallel, \text{in}, 0} + i \frac{x}{g} \tilde{\phi} \quad (\text{A9})$$

$$\Leftrightarrow \quad \tilde{A}_{\parallel, \text{in}, 1}'' = \kappa \left(\tilde{A}_{\parallel, \text{in}, 0} - x \left(-i \frac{\tilde{\phi}}{g} \right) \right). \quad (\text{A10})$$

Without loss of generality we can set $\tilde{A}_{\parallel, \text{in}, 0} = 1$ and obtain

$$\tilde{A}_{\parallel, \text{in}, 1}'' = \kappa (1 - x \tilde{\xi}) \quad (\text{A11})$$

where we defined the displacement function $\tilde{\xi} = -i\tilde{\phi}/g$ ⁴⁴. At this point it is helpful to rewrite κ and defining new quantities

$$\begin{aligned} \varphi^{-1} &:= N_0^2 \left(1 - \mu_e \left(1 + \frac{2}{\beta N_0} \right) \right) \\ \lambda &= \beta^2 (A_0^2 \mu_e + N_0^2) \\ \kappa &= \frac{N_0 (g^2 N_0 (\beta N_0 - \mu_e (2 + \beta N_0)) + \beta^3 (A_0^2 \mu_e + N_0^2) x^2)}{-g^2 \mu_e N_0^2 + \beta^2 (A_0^2 \mu_e + N_0^2) x^2} = \\ \kappa &= \frac{N_0 \beta (g^2 N_0^2 (1 - \mu_e (1 + \frac{2}{\beta N_0})) + \beta^2 (A_0^2 \mu_e + N_0^2) x^2)}{-g^2 \mu_e N_0^2 + \beta^2 (A_0^2 \mu_e + N_0^2) x^2} = \\ \kappa &= \frac{N_0 \beta (g^2 \varphi^{-1} + \lambda x^2)}{-g^2 \mu_e N_0^2 + \lambda x^2} = \\ &= N_0 \beta \frac{g \varphi^{-1} + \frac{\lambda}{g} x^2}{(-g \mu_e N_0^2) + \frac{\lambda}{g} x^2} = \\ &= N_0 \beta \frac{\frac{g \varphi^{-1}}{\lambda} + \frac{x^2}{g}}{\frac{(-g \mu_e N_0^2)}{\lambda} + \frac{x^2}{g}} = \\ &= N_0 \beta \frac{\sigma + \frac{x^2}{\delta^2}}{\varepsilon + \frac{x^2}{\delta^2}} \end{aligned}$$

where we introduce: $\delta := \sqrt{g}$ as a renormalization factor, the parameter $\sigma := g \varphi^{-1} \lambda^{-1}$ and the expansion parameter $\varepsilon := -g N_0^2 (\mu_e) \lambda^{-1}$. We now want to first solve the ODE for ϕ or $\xi(x)$. So we use equation 7^x to eliminate \tilde{A}_{\parallel}

$$\tilde{A}_{\parallel, \text{in}} = N_0 \beta \frac{\sigma + \frac{x^2}{\delta^2}}{\varepsilon + \frac{x^2}{\delta^2}} (1 - x \tilde{\xi}) = \frac{ig \tilde{\phi}''}{x \beta} N_0 \quad (\text{A12})$$

and after transformation of

$$i \frac{g}{x} \tilde{\phi}'' = \beta^2 \frac{\sigma + \frac{x^2}{\delta^2}}{\varepsilon + \frac{x^2}{\delta^2}} \left(1 - x (-1) \frac{\tilde{\phi}}{g} \right)$$

$$-\frac{g^2}{x} \tilde{\xi}'' = \beta^2 \frac{\sigma + \frac{x^2}{\delta^2}}{\varepsilon + \frac{x^2}{\delta^2}} \left(1 - x \tilde{\xi} \right)$$

$$\frac{g^2}{x} \tilde{\xi}'' = -\beta^2 \frac{\sigma + \frac{x^2}{\delta^2}}{\varepsilon + \frac{x^2}{\delta^2}} \left(1 - x \tilde{\xi} \right)$$

$$\frac{g^2}{x} \tilde{\xi}'' = \beta^2 \frac{\sigma + \frac{x^2}{\delta^2}}{\varepsilon + \frac{x^2}{\delta^2}} \left(x \tilde{\xi} - 1 \right)$$

with

$$z := \frac{x}{\delta}, \quad \hat{\xi}(z) := \delta \tilde{\xi}(\delta z), \quad (\text{A13})$$

$$\begin{aligned} \Rightarrow \quad \hat{\xi}''(z) &= \delta \frac{d^2}{dz^2} \tilde{\xi}(x) \\ &= \delta \frac{d}{dz} \left(\frac{dx}{dz} \frac{d}{dx} \tilde{\xi}(x) \right) \\ &= \delta^2 \frac{dx}{dz} \frac{d}{dx} \tilde{\xi}'(x) \\ &= \delta^3 \tilde{\xi}''(x), \end{aligned}$$

This equation turns into a second order differential equation in z for $\hat{\xi}$

$$\frac{g^2}{\delta^3} \hat{\xi}''(z) = \frac{\delta^4}{\delta^3} \tilde{\xi}''(z) = \beta^2 z \delta (z \hat{\xi} - 1) \frac{z^2 + \sigma}{z^2 + \varepsilon} \quad (\text{A14})$$

$$\hat{\xi}''(z) = \beta^2 z (z \hat{\xi} - 1) \frac{z^2 + \sigma}{z^2 + \varepsilon}. \quad (\text{A15})$$

This differential equation can be solved analytically in the case where $\varepsilon \ll \sigma \ll 1$ ordering is applied (large z ordering)

$$\hat{\xi}'' = -\beta^2 z + \beta^2 \hat{\xi} z^2 \quad (\text{A16})$$

and the boundary conditions

$$\hat{\xi}(0) = 0, \quad \lim_{x \rightarrow \infty} \hat{\xi}(x) = x^{-1}$$

apply. The solution, given by Goldston, Rutherford and Furth, is³⁸

$$\hat{\xi}(z) = \beta \frac{z}{2} \int_0^{\pi/2} \exp\left(-\beta \frac{z^2}{2} \cos(\theta)\right) \sin^{1/2}(\theta) d\theta. \quad (\text{A17})$$

Having an expression for $\hat{\xi}$ we now can try to solve the integral for the matching parameter, making use of the relation for \tilde{A}_{\parallel} (eq. A12)

$$\Delta' = \int_{-\infty}^{\infty} dx \tilde{A}_{\parallel}'' = \quad (\text{A18})$$

$$= \int_{-\infty}^{\infty} dx N_0 \beta \frac{\sigma + \frac{x^2}{\delta^2}}{\varepsilon + \frac{x^2}{\delta^2}} (1 - x \tilde{\xi}) = \quad (\text{A19})$$

$$= \int_{-\infty}^{\infty} dz \delta N_0 \beta (1 - z \hat{\xi}) \frac{z^2 + \sigma}{z^2 + \varepsilon} \quad (\text{A20})$$

An expression for $\tilde{A}''_{||,in,1}$ was obtained by substituting via equation (A13) the integral can be rearranged to

$$\begin{aligned}\Delta'_{inner} &= \beta N_0 \int_{-\infty}^{\infty} \frac{(x/\delta)^2 + \sigma}{(x/\delta)^2 + \varepsilon} \left(1 - \frac{x}{\delta} \delta \tilde{\xi}(x)\right) \\ &= \beta N_0 \delta \int_{-\infty}^{\infty} \frac{z^2 + \sigma}{z^2 + \varepsilon} \left(1 - z \hat{\xi}(z)\right) dz \\ &= \beta N_0 \delta \int_{-\infty}^{\infty} \left(1 + \frac{\sigma}{\varepsilon} \frac{1}{1+z^2/\varepsilon} - \frac{1}{1+z^2/\varepsilon}\right) \left(1 - z \hat{\xi}(z)\right) dz \\ &=: \beta N_0 \delta \left(I_1 + \left(\frac{\sigma - \varepsilon}{\varepsilon}\right) I_2\right),\end{aligned}$$

The main contribution to the integral is in the regions for $|z| > \sigma$ or $z^2 \gg \sigma \gg \varepsilon$. Evaluating the first Integral one finds^{45,69}

$$\begin{aligned}I_1 &= \int_{-\infty}^{\infty} (1 - z \hat{\xi}(z)) dz \\ &\approx \frac{2.12}{\sqrt{\beta}}\end{aligned}$$

which can be tested by numerical evaluation of the integral. Outside of the region $z \in [-\sigma, \sigma]$ the function

$$f_2(z) = \frac{1}{1+z^2/\varepsilon}$$

practically vanishes and suppresses every function it gets multiplied to. Thus the function $f_2(z) (1 - z \hat{\xi}(z))$ is only non-zero inside this region. Together with the leading order solution valid for $|z| \lesssim \sigma/\alpha$ (has been numerically tested by us for small ε) one concludes

$$\begin{aligned}I_2 &= \int_{-\infty}^{\infty} \frac{1 - z \hat{\xi}(z)}{1 + z^2/\varepsilon} dz \\ &\approx \pi \varepsilon^{1/2}.\end{aligned}\quad (\text{A21})$$

$$\Delta'_{inner} = \beta N_0 \delta \left(\frac{2.12}{\sqrt{\beta}} + \left(\frac{\sigma - \varepsilon}{\varepsilon} \right) \pi \varepsilon^{1/2} \right).\quad (\text{A22})$$

Substituting the definitions one finally gets

$$\begin{aligned}\Delta'_{outer} &= 2 \left(\frac{1}{k} - k \right) = \Delta'_{inner} = \\ &= \beta N_0 \sqrt{\left(\frac{\gamma_{in}}{A_0 k} \right)} \left[\frac{2.12}{\sqrt{\beta}} + \pi \left(\frac{\frac{1}{\phi} + \mu_e N_0^2}{-\mu_e N_0^2} \right) \left(\frac{\gamma - \mu_e N_0^2}{\lambda A_0 k} \right)^{1/2} \right]\end{aligned}\quad (\text{A23})$$

¹A. H. Boozer, "Why fast magnetic reconnection is so prevalent," *Journal of Plasma Physics* **84** (2018), <http://doi.org/10.1017/S0022377818000028>, Cambridge University Press.

²E. G. Zweibel and M. Yamada, "Perspectives on magnetic reconnection," *Proc. R. Soc. A* **472** (2016), <https://doi.org/10.1098/rspa.2016.0479>, Royal Society Publishing.

³A. Letsch, H. Zohm, F. Ryter, W. Suttrop, A. Gude, F. Porcelli, C. Angioni, and I. Furno, "Incomplete reconnection in sawtooth crashes in ASDEX upgrade," *Nuclear Fusion* **42** (2002), iOP Publishing.

⁴E. N. Parker, "The generation of magnetic fields in astrophysical bodies. i. the dynamo equations," *Astrophysical Journal* **162**, 665 (1970), Institute of Physics Publishing.

⁵E. N. Parker, "Sweet's mechanism for merging magnetic fields in conducting fluids," *Journal of Geophysical Research* **62**, 509–520 (1970), Wiley.

⁶H. E. Petschek, AAS/NASA Symposium on the Physics of Solar Flares **2372**, 425 (1964), NASA Washington DC.

⁷D. Uzdensky, N. F. Loureiro, and A. A. Schekochihin, "Fast magnetic reconnection in the plasmoid-dominated regime," *PHYSICAL REVIEW LETTERS* **105** (2010), <https://doi.org/10.1103/PhysRevLett.105.1500>.

⁸N. Loureiro, A. A. Schekochihin, and S. C. Cowley, "Instability of current sheets and formation of plasmoid chains," *Physics of Plasmas* **14** (2007).

⁹H. Baty, "On the onset of the plasmoid instability," *Physics of Plasmas* **19**, 092110 (2012), https://pubs.aip.org/aip/pop/article-pdf/doi/10.1063/1.4752744/16124733/092110_1_online.pdf.

¹⁰A. Bhattacharjee, H. Yi-Min, H. Yang, and B. Rogers, "Fast reconnection in high-lundquist-number plasmas due to the plasmoid instability," *Physics of Plasmas* **16** (2009), <https://doi.org/10.1063/1.3264103>, AIP Publishing.

¹¹L. Comisso and D. Grasso, "Visco-resistive plasmoid instability," *Physics of Plasmas* **23** (2016), <https://doi.org/10.1063/1.4942940>, AIP Publishing.

¹²L. Comisso, M. Lingam, Y.-M. Huang, and A. Bhattacharjee, "General theory of the plasmoid instability," *Phys. of Plasmas* **23** (2016), <https://doi.org/10.1063/1.4964481>.

¹³L. Ni, U. Ziegler, Y.-M. Huang, J. Lin, and Z. Mei, "Effects of plasma β on the plasmoid instability," *Physics of Plasmas* **19**, 072902 (2012), https://pubs.aip.org/aip/pop/article-pdf/doi/10.1063/1.4736993/16114983/072902_1_online.pdf.

¹⁴F. Pucci and M. Velli, "Reconnection of quasi-singular current sheets: the "ideal" tearing mode," *The Astrophysical Journal Letters* **780**, L19 (2013).

¹⁵Y.-M. Huang, L. Comisso, and A. Bhattacharjee, "Plasmoid instability in evolving current sheets and onset of fast reconnection," *The Astrophysical Journal* **849**, 75 (2017).

¹⁶L. Comisso and D. Grasso, "Visco-resistive plasmoid instability," *Physics of Plasmas* **23** (2016).

¹⁷J. M. G. Morillo and A. Alexakis, "Magnetic reconnection, plasmoids and numerical resolution," *Journal of Fluid Mechanics* **1007**, R3 (2025).

¹⁸A. H. Boozer, "Physics of magnetically confined plasmas," *Rev. Mod. Phys.* **76**, 1071–1141 (2005).

¹⁹T. Oikawa, A. Isayama, T. Fujita, T. Suzuki, T. Tuda, and G. Kurita, "Evolution of the current density profile associated with magnetic island formation in JT-60U," *Phys. Rev. Lett.* **94**, 125003 (2005).

²⁰W. Tae, E. Yoon, M. S. Hur, G. Choi, J. Kwon, and M. Choi, "Unveiling non-flat profiles within magnetic islands in tokamaks," *Physics of Plasmas* **31** (2024).

²¹A. Ishizawa, Y. Kishimoto, and Y. Nakamura, "Multi-scale interactions between turbulence and magnetic islands and parity mixture—a review," *Plasma Physics and Controlled Fusion* **61**, 054006 (2019).

²²Y.-M. Huang and A. Bhattacharjee, "Scaling laws of resistive magnetohydrodynamic reconnection in the high-lundquist-number, plasmoid-unstable regime," *Physics of Plasmas* **17**, 062104 (2010), https://pubs.aip.org/aip/pop/article-pdf/doi/10.1063/1.3420208/16029914/062104_1_online.pdf.

²³C. Dong, L. Wang, Y.-M. Huang, L. Comisso, and A. Bhattacharjee, "Role of the plasmoid instability in magnetohydrodynamic turbulence," *Phys. Rev. Lett.* **121**, 165101 (2018).

²⁴M. Ottavini and F. Porcelli, "Nonlinear collisionless magnetic reconnection," *Phys. Rev. Lett.* **71** (1993), <https://doi.org/10.1103/PhysRevLett.71.3802>.

²⁵D. Grasso, F. Califano, F. Pegoraro, and F. Porcelli, "Ion larmor radius effects in collisionless reconnection," *Plasma Phys. Rep.*, 512–518 (2000).

²⁶L. Comisso, D. Grasso, F. L. Waelbroeck, and D. Borgogno, "Gyro-induced acceleration of magnetic reconnection," *Phys. Plasmas* **60** (2013), <https://doi.org/10.1063/1.4821840>.

²⁷A. Biancalani and B. Scott, "Observation of explosive collisionless reconnection in 3d nonlinear gyrofluid simulations," *EPL* **97** (2012), <https://doi.org/10.1209/0295-5075/97/15005>.

²⁸B. Scott, "Derivation via free energy conservation constraints of gyrofluid equations with finite-gyroradius electromagnetic nonlinearities," *Phys. Plasmas* **17** (2010), <https://doi.org/10.1063/1.3484219>.

²⁹M. A. Shay, J. F. Drake, B. N. Rogers, and R. E. Denton, "The scaling of

- collisionless, magnetic reconnection for large systems,” *Geophysical Research Letters* **26**, 2163–2166 (1999), canonical kinetic reconnection study with fast rates.
- ³⁰J. Birn, J. F. Drake, M. A. Shay, and et al., “Geospace environmental modeling (gem) magnetic reconnection challenge,” *Journal of Geophysical Research* **106**, 3715–3720 (2001), hall and kinetic models in GEM challenge, fast reconnection.
- ³¹R. Numata, W. Dorland, G. G. Howes, N. F. Loureiro, B. N. Rogers, and T. Tatsuno, “Gyrokinetic simulations of the tearing instability,” *Physics of Plasmas* **18**, 112106 (2011), gyrokinetic tearing reconnection studies relevant to fast rates.
- ³²M. Yamada, R. Kulsrud, and H. Ji, “Magnetic reconnection,” *Reviews of Modern Physics* **82**, 603–664 (2010), comprehensive reconnection review.
- ³³C. Granier, D. Borgogno, D. Grasso, and E. Tassi, “Gyrofluid analysis of electron β_e effects on collisionless reconnection,” *Journal of Plasma Physics* **88**, 905880111 (2022).
- ³⁴F. Locker, M. Held, T. Stocker-Waldhuber, A. Stürz, M. Rinner, and A. Kendl, “Greeny: A full-f 2d gyrofluid reconnection code,” *Computer Physics Communications*, 109807 (2025).
- ³⁵A. Kendl, “Tiff: Gyrofluid turbulence in full-f and full-k,” *Computer Physics Communications* **294** (2023), <https://doi.org/10.1016/j.cpc.2023.108953>.
- ³⁶M. Held, M. Wiesenberger, and A. Kendl, “The collisional drift wave instability in steep density gradient regimes,” *Nucl. Fusion* **59** (2019), <https://doi.org/10.1088/1741-4326/aaf6cc>.
- ³⁷J. Madsen, “Full-f gyrofluid model,” *Phys. Plasmas* **20** (2013), <https://doi.org/10.1063/1.4813241>.
- ³⁸B. Scott, *Turbulence and Instabilities in Magnetised Plasmas: Volume 2* (IOP Publishing, 2021).
- ³⁹M. Held, M. Wiesenberger, and A. Kendl, “Padé-based arbitrary wavelength polarization closures for full-f gyro-kinetic and -fluid models,” *Nucl. Fusion* **60** (2020), <https://doi.org/10.1088/1741-4326/ab7a68>.
- ⁴⁰M. Held and M. Wiesenberger, “Beyond the oberbeck–boussinesq and long wavelength approximation,” *Nucl. Fusion* **63** (2022), <https://doi.org/10.1088/1741-4326/aca9e0>.
- ⁴¹S. Smith and G. Hammett, “Eddy viscosity and hyperviscosity in spectral simulations of 2d drift wave turbulence,” *Physics of Plasmas* **4**, 978–990 (1997).
- ⁴²B. D. Scott, “The mechanism of self-sustainment in collisional drift wave turbulence,” *Physics of Fluids B: Plasma Physics* **4**, 2468–2494 (1992).
- ⁴³S. J. Camargo, M. K. Tippet, and I. L. Caldas, “Nonmodal energetics of electromagnetic drift waves,” *Physics of Plasmas* **7**, 2849–2855 (2000).
- ⁴⁴E. Tassi, D. Grasso, and L. Comisso, “Linear stability analysis of collisionless reconnection in the presence of an equilibrium flow aligned with the guide field,” *Eur. Phys. J. D* **68** **88** (2014), <https://doi.org/10.1140/epjd/e2014-40730-6>.
- ⁴⁵H. P. Furth, J. Killeen, and M. N. Rosenbluth, “Finite-resistivity instabilities of a sheet pinch,” *Physics of Fluids* **6** (1963), <https://doi.org/10.1063/1.1706761>.
- ⁴⁶A. Glasser, J. Greene, and J. Johnson, “Resistive instabilities in general toroidal plasma configurations,” *The Physics of Fluids* **18**, 875–888 (1975).
- ⁴⁷D. Biskamp and D. Biskamp, *Nonlinear magnetohydrodynamics*, 1 (Cambridge University Press, 1997).
- ⁴⁸L. N. Trefethen, “Spectra and pseudospectra,” (Springer, 2001) ISBN: 0387989854.
- ⁵⁰L. N. Trefethen, “Pseudospectra of linear operators,” *SIAM REV.* **39**, 383–406 (1997).
- ⁵¹S. J. Camargo, M. K. Tippet, and I. L. Caldas, “Nonmodal energetics of resistive drift waves,” *PHYSICAL REVIEW E* **85**, **3** (1998), <https://doi.org/10.1103/PhysRevE.58.3693>.
- ⁵²B. Friedman and T. Carter, “A non-modal analytical method to predict turbulent properties applied to the hasegawa-wakatani model,” *PHYSICS OF PLASMAS* **22** (2015), <https://doi.org/10.1063/1.4905863>.
- ⁵³L. N. Trefethen, A. E. Trefethen, S. C. Reddy, and T. A. Driscoll, “Hydrodynamic stability without eigenvalues,” *Science* **261**, 578–584 (1993), <http://www.jstor.org/stable/2882016>.
- ⁵⁴D. MacTaggart, “The non-modal onset of the tearing instability,” *J. Plasma Phys.* **84** (2018), <https://doi.org/10.1017/S0022377818001009>.
- ⁵⁵M. Hirota, “An explosive scaling law for nonlinear magnetic reconnection and its insensitivity to microscopic scales,” *Plasma and Fusion Research* **12** (2017), <https://doi.org/10.1585/pfr.12.1401010>, jSPF.
- ⁵⁶F. F. Locker, *2D Full-F Gyrofluid Magnetic Reconnection*, Phd thesis, University of Innsbruck, Innsbruck (2025), available at <https://u1b-dok.uibk.ac.at/>.
- ⁵⁷Wolfram Research, Inc., “Mathematica, version 12.3,” (2024).
- ⁵⁸L. N. Trefethen, M. Contedini, and M. Embree, “Spectra, pseudospectra, and localization for random bidiagonal matrices,” *Communications on Pure and Applied Mathematics* **LIV**, 0595–0623 (2001), John Wiley and Sons.
- ⁵⁹A. Y. Aydemir, “Nonlinear studies of $m=1$ modes in high-temperature plasmas,” *Phys. Fluids B*, **4**, 3469–3472 (1992).
- ⁶⁰A. Stanier, A. N. Simakov, L. Chacón, and W. Daughton, “Fluid vs. kinetic magnetic reconnection with strong guide fields,” *Phys. Plasmas* **22** (2015), <https://doi.org/10.1063/1.4932330>.
- ⁶¹C. Granier, R. Numata, D. Borgogno, E. Tassi, and D. Grasso, “Investigation of the collisionless plasmoid instability based on gyrofluid and gyrokinetic integrated approach,” *J. Plasma Phys.* **89** (2023), <https://doi.org/10.1017/S0022377823000570>.
- ⁶²F. Porcelli, D. Borgogno, F. Califano, D. Grasso, M. Ottaviani, and F. Pegoraro, “Recent advances in collisionless magnetic reconnection,” *Plasma physics and controlled fusion* **44**, B389 (2002).
- ⁶³E. Priest, “Other topological invariants and braiding experiments,”.
- ⁶⁴M. Wiesenberger and H. M., “Feltor,” <https://github.com/feltor-dev> (2024).
- ⁶⁵C. Hirsch, *Numerical computation of internal and external flows: The fundamentals of computational fluid dynamics* (Elsevier, 2007).
- ⁶⁶Y.-H. Liu, P. Cassak, X. Li, M. Hesse, S.-C. Lin, and K. Genestreti, “First-principles theory of the rate of magnetic reconnection in magnetospheric and solar plasmas,” *Communications Physics* volume **5** **5** (2022), <https://doi.org/10.1038/s42005-022-00854-x>.
- ⁶⁷D. Biskamp, “Magnetic reconnection in plasmas,” *Astrophysics and Space Science* **242**, 165–207 (1996).
- ⁶⁸R. Fitzpatrick and F. L. Waelbroeck, “Drift-tearing magnetic islands in tokamak plasmas,” *Phys. Plasmas* **15** (2008), <https://doi.org/10.1063/1.2829757>.
- ⁶⁹M. N. Bussac, D. Edery, R. Pellat, and J. L. Soule, “Stabilization of the linear drift tearing mode by coupling with the ion sound wave,” *PHYSICAL REVIEW LETTERS* **40** (1978), <https://doi.org/10.1103/PhysRevLett.40.1500>.
- ⁴⁹P. J. Schmid and D. S. Hennington, *Stability and Transition in Shear Flows*